Journal of Computational Physics 228 (2009) 4917–4944

Contents lists available at ScienceDirect

Journal of Computational Physics

journal homepage: www.elsevier.com/locate/jcp

Multi-dimensional conservative semi-Lagrangian method of characteristics CIP for the shallow water equations

Kunihiko Toda [a], Youichi Ogata [b,*], Takashi Yabe [a,c]

[a] Department of Mechanical Science and Engineering, Tokyo Institute of Technology, 2-12-1, O-Okayama, Meguro-ku, Tokyo 152-8552, Japan
[b] Department of Mechanical System Engineering, Hiroshima University, 1-4-1, Kagamiyama, Higashi-Hiroshima-shi 739-8527, Japan
[c] Integrated Research Institute, Solutions Research Organization, Tokyo Institute of Technology, 2-12-1, O-Okayama, Meguro-ku, Tokyo 152-8552, Japan

ARTICLE INFO

Article history:
Received 20 June 2008
Received in revised form 30 March 2009
Accepted 2 April 2009
Available online 16 April 2009

Keywords:
CIP method
Conservation
Semi-Lagrangian
Shallow water equations
Method of characteristics

ABSTRACT

A new characteristic approach that guarantees conservative property is proposed and is applied to the shallow water equations. CIP–CSL (Constrained Interpolation Profile/Conservative Semi-Lagrangian) interpolation is applied to the CIP method of characteristics in order to enhance the mass conservation of the numerical result. Although the characteristic formulation is originally derived from non-conservative form, present scheme achieves complete mass conservation by solving mass conservation simultaneously and reflecting conserving mass in interpolation profile. Present method has less height error compared to the CIP method of characteristics by several orders of magnitude. By the enhanced conservation property, present scheme is applicable to nonlinear problem such as shock. Furthermore, application to two dimensions including the Coriolis term is straightforward with directional splitting technique.

1. Introduction

The shallow water equations are often used for benchmark problems of new schemes in numerical weather prediction and have been extensively studied in various forms [1,2]. Conservative schemes essentially warrant the conservation of height while the time step interval Δt is strictly limited to be short by large acceleration of the gravity term. The strict time step interval constraint has been a problem in explicit Eulerian representations, due to the fast gravity waves [3].

The characteristic approach [4] is, however, at liberty to choose a large time step interval Δt because the speed of the gravity wave is included in the advection speed of Riemann invariants, and the Courant–Friedrichs–Lewy (CFL) constraint from gravity term can be removed with such semi-Lagrangian approaches. The application of the CIP method [5,6] to the semi-Lagrangian characteristic approach proved its high efficiency and accuracy [7], however, its lack of conservation remains unresolved because the characteristics formulation is derived from a non-conservative form.

In simulations of the whole Earth, for example, the volume of seawater is about 1.37×10^9 [km^3]. Therefore, although the CIP method shows good conservation of mass, the actual error of seawater volume becomes tremendous. Besides, from the viewpoint of numerical schemes, exact mass conservation is essential in order to accurately calculate shock problems or long-term simulations [8].

While semi-Lagrangian approaches have made computations greatly efficient in a variety of fields, the lack of conservation has always been pointed out. Some excellent conserving semi-Lagrangian schemes have been proposed, such as

* Corresponding author.
E-mail addresses: toda.k.aa@m.titech.ac.jp (K. Toda), yogata@hiroshima-u.ac.jp (Y. Ogata), yabe@mech.titech.ac.jp (T. Yabe).

0021-9991/$ - see front matter © 2009 Elsevier Inc. All rights reserved.
doi:10.1016/j.jcp.2009.04.003

semi-Lagrangian Inherently Conserving and Efficient (SLICE) [9,10], Cell-Integrated Semi-Lagrangian (CISL) [11], semi-Implicit Locally Mass Conserving semi-Lagrangian (SI-LMCSL) [12] schemes, Finite Volume Method (FVM)-based scheme [13,14] or CIP–FVM scheme [15], and they have been also used for numerical weather prediction models through the shallow water equations. In the past several years, one of authors developed the Conservative Semi-Lagrangian (CSL) scheme based on the CIP method and it has been applied to various kinds of problems [16–20].

In this paper, we propose a new conservative scheme by adopting the CIP–CSL scheme to the method of characteristics (MOC) and examine its characteristics with the shallow water equations in multi-dimensions.

This paper is organized of the following sections. Section 2 explains interpolation methods to transport Riemann invariants. In Section 3, the CIP and the CIP–CSL interpolations are applied to the transport of Riemann invariants in one-dimensional shallow water equations and the present method is tested in linear and shock problems. Applications of the present method to large CFL numbers are also demonstrated and discussed. In Section 4, the present method is extended to two dimensions and tested with various problems. Conclusion and discussion are given in Section 5.

2. Interpolation methods

The solution of an advection equation

$$\frac{\partial f}{\partial t} + u\frac{\partial f}{\partial x} = 0, \tag{1}$$

is a simple advection of profile f with the characteristic velocity u as follows:

$$f(x, t + \Delta t) = f(x - u\Delta t, t), \tag{2}$$

when u is constant. Even if u is a function of time t and space x, we can locally use the solution equation (2) as follows:

$$f(x_i, t + \Delta t) = f(x_i - u_i\Delta t, t), \tag{3}$$

where x_i and u_i are the grid point and the velocity at x_i, respectively. Thus it can be accurately solved by interpolating the upstream departure point $x_i - u\Delta t$ with an accurate approximation. By diagonalizing or transforming the vector–matrix form of the shallow water equations [21], they become a set of simple advection equations for Riemann invariants. Here we introduce three interpolation methods to transport the Riemann invariants.

2.1. CIP interpolation

We shall briefly describe the CIP method, which is a robust and less diffusive solver for hyperbolic equation with accuracy of third order both in time and space. Let us consider the solution of the hyperbolic equation first. The equation for the first spatial derivative is derived from Eq. (1)

$$\frac{\partial(\partial_x f)}{\partial t} + u\frac{\partial(\partial_x f)}{\partial x} = -\partial_x f\frac{\partial u}{\partial x}, \tag{4}$$

where we denote $\partial_x \equiv \partial/\partial x$. The right hand side of Eq. (4) vanishes when u is constant, and the solution of Eq. (4) at the grid point x_i is given by

$$\partial_x f(x_i, t + \Delta t) = \partial_x f(x_i - u\Delta t, t). \tag{5}$$

Eq. (5) means that the spatial derivative of f also travels with the velocity of u, along with the profile. Since the upstream departure point $x_i - u\Delta t$ is not usually at a grid point, we need to interpolate the value at the upstream departure point with values on grid points. The CIP method constructs a cubic polynomial interpolation with values and spatial derivatives at the both adjacent side grid points (Fig. 1). Thus, the value and spatial derivative at the $(n+1)$ step are obtained by shifting the profile by $u_i\Delta t$ as follows:

$$f_i^{n+1} = F_i(x_i - u_i\Delta t) = a_i\xi^3 + b_i\xi^2 + \partial_x f_i\xi + f_i, \tag{6}$$

$$\partial_x f_i^{n+1} = \partial_x F_i(x_i - u_i\Delta t) = 3a_i\xi^2 + 2b_i\xi + \partial_x f_i, \tag{7}$$

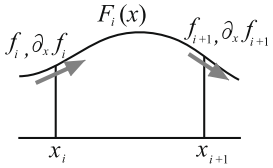

Fig. 1. Schematic of CIP interpolation.

$$a_i = \frac{(\partial_x f_i + \partial_x f_{iup})}{D^2} + \frac{2(f_i - f_{iup})}{D^3}, \tag{8}$$

$$b_i = \frac{3(f_{iup} - f_i)}{D^2} - \frac{(2\partial_x f_i + \partial_x f_{iup})}{D}, \tag{9}$$

where $\xi = -u_i\Delta t,\ iup = i - \mathrm{sgn}(u_i),\ \mathrm{sgn}(u_i) = 1\ (u_i \geqslant 0),\ -1\ (u_i < 0),\ D = -\Delta x \cdot \mathrm{sgn}(u_i),\ \partial_x f \equiv \partial f/\partial x$. In the case u changes, the third term in Eq. (4) must be solved with finite difference additionally [5]. It has already been proved in previous literatures [22,16,7] that the CIP method has extremely low dispersion error and numerical damping.

2.2. CIP–CSL4 interpolation

The CIP–CSL4 [17–19] scheme is almost the same as the CIP method but requires that an integral of an interpolation profile is equivalent to a cell mass between grid points (Fig. 2). With the value f and the spatial derivative $\partial_x f$ defined on a grid point like collocated grid and the cell mass $\rho \equiv \int F(x,t)dx$ defined at the center of the cell like staggered grid, we can construct a quartic polynomial interpolation profile between two grid points:

$$f_i^{n+1} = F_i(x_i - u\Delta t) = a_i\xi^4 + b_i\xi^3 + c_i\xi^2 + \partial_x f_i\xi + f_i, \tag{10}$$

$$\partial_x f_i^{n+1} = \partial_x F_i(x_i - u\Delta t) = 4a_i\xi^3 + 3b_i\xi^2 + 2c_i\xi + \partial_x f_i, \tag{11}$$

$$a_i = \frac{-5\left(6(f_{iup} + f_i)D - (\partial_x f_{iup} - \partial_x f_i)D^2 + 12\mathrm{sgn}(u_i^n)\rho_{icell}\right)}{2D^5}, \tag{12}$$

$$b_i = \frac{4\left((7f_{iup} + 8f_i)D - (\partial_x f_{iup} - (3/2)\partial_x f_i)D^2 + 15\mathrm{sgn}(u_i^n)\rho_{icell}\right)}{D^4}, \tag{13}$$

$$c_i = \frac{-3\left(4(2f_{iup} + 3f_i)D - (\partial_x f_{iup} - 3\partial_x f_i)D^2 + 20\mathrm{sgn}(u_i^n)\rho_{icell}\right)}{2D^3}. \tag{14}$$

Here, $icell = i - \mathrm{sgn}(u_i)/2$ and $\rho_{i+1/2} = \int_{x_i}^{x_{i+1}} F_i(x)dx$.

2.3. CIP–CSL2 interpolation

The CIP–CSL2 [17,20] scheme as well as the CSL4 scheme also require that the integral of interpolation profile is equivalent to the cell mass, however, without spatial derivatives. The interpolation profile is approximated as follows:

$$f_i^{n+1} = F(x_i - u_i\Delta t) = 3a_i\xi^2 + 2b_i\xi + f_i, \tag{15}$$

$$a_i = \frac{f_i + f_{iup}}{D^2} + \frac{2\mathrm{sgn}(u_i)\rho_{icell}}{D^3}, \tag{16}$$

$$b_i = -\frac{2f_i + f_{iup}}{D} - \frac{3\mathrm{sgn}(u_i)\rho_{icell}}{D^2}. \tag{17}$$

The time development of the cell mass ρ is also needed in CIP–CSL schemes, which can be calculated by considering the flux $\Delta\rho_i$ passing through x_i during $[t, t + \Delta t]$ as follows (see Figs. 4 and 5 in Section 3):

$$\rho_{i+1/2}^{n+1} = \rho_{i+1/2}^n + \Delta\rho_i - \Delta\rho_{i+1}. \tag{18}$$

The way of estimation of $\Delta\rho_i$ in CSL–MOC schemes is given in Section 3.

3. One-dimensional shallow water equations

3.1. Characteristic formulation and discretization

Let h be the water height above a bottom, u the velocity and g the gravitational acceleration, then the one-dimensional shallow water equations in a primitive form are written as

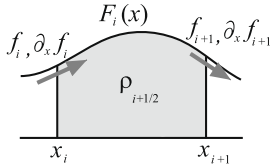

Fig. 2. Schematic of CSL4 interpolation.

$$\frac{\partial h}{\partial t}+\frac{\partial (uh)}{\partial x}=0, \tag{19}$$

$$\frac{\partial u}{\partial t}+u\frac{\partial u}{\partial x}+g\frac{\partial h}{\partial x}=0. \tag{20}$$

The effect of a bottom topography can be also included as the source term in the shallow water equations. The extension will be given in the Appendix.

If let L_0 and h_0 be the characteristic length and height of the system, U_0 be the characteristic velocity and $t_0 = L_0/U_0$ be time, hereafter we can use Eqs. (19) and (20) as nondimensional basic equations. The corresponding Froude number $Fr\left(\equiv U_0/\sqrt{gh_0}\right)$ can be defined as $g \equiv 1/Fr^2$ in Eq. (20).

In a vector–matrix form, Eqs. (19) and (20) are rewritten as

$$\frac{\partial}{\partial t}\begin{pmatrix} h \\ u \end{pmatrix}+\begin{pmatrix} u & h \\ g & u \end{pmatrix}\frac{\partial}{\partial x}\begin{pmatrix} h \\ u \end{pmatrix}\equiv \frac{\partial \mathbf{W}}{\partial t}+\mathbf{A}(\mathbf{W})\frac{\partial \mathbf{W}}{\partial x}=0. \tag{21}$$

With a matrix $\mathbf{L}$ which diagonalizes the matrix $\mathbf{A}$ as $\mathbf{L}^{-1}\mathbf{A}\mathbf{L}$, Eq. (21) can be written as

$$\mathbf{L}^{-1}\frac{\partial \mathbf{W}}{\partial t}+(\mathbf{L}^{-1}\mathbf{A}\mathbf{L})\mathbf{L}^{-1}\frac{\partial \mathbf{W}}{\partial x}=0, \tag{22}$$

where $\mathbf{L}^{-1}$ is the inverse matrix of $\mathbf{L}$, and $C^{\pm}$ are the eigenvalues of $\mathbf{A}$, respectively, and they can be simply given as follows:

$$C^{\pm}=u\pm\Gamma, \tag{23}$$

$$\mathbf{L}=\begin{pmatrix} 1 & 1 \\ \sqrt{gh} & -\sqrt{gh} \end{pmatrix},\quad \mathbf{L}^{-1}=\frac{1}{2}\begin{pmatrix} 1 & \sqrt{h/g} \\ 1 & -\sqrt{h/g} \end{pmatrix}, \tag{24}$$

where $\Gamma=\sqrt{gh}$. If $\mathbf{A}(\mathbf{W})$ is a constant matrix (the linear shallow water equations), Eq. (22) can be exactly diagonalized. However, even if $\mathbf{A}(\mathbf{W})$ is not the constant matrix (the nonlinear shallow water equations as Eq. (21)), Eq. (22) can be rewritten in the following simpler form [4],

$$\frac{\partial R^{\pm}}{\partial t}+C^{\pm}\frac{\partial R^{\pm}}{\partial x}=0, \tag{25}$$

where $R^{\pm}=\Gamma\pm u/2$ are called the Riemann invariants. Eq. (25) means that the Riemann invariants propagate with the speed of $u\pm\Gamma$ (see Fig. 3). Eq. (25) (or Eq. (22)) is in a form favorable to the CIP method because they are (despite nonlinear equations) pure advection equations. Since the CIP method needs not only values but also spatial derivatives, we also need to solve spatial derivatives of the Riemann invariants. Taking the spatial derivative of Eq. (25) leads to ()

$$\frac{\partial}{\partial t}(\partial_x R^{\pm})+C^{\pm}\frac{\partial}{\partial x}(\partial_x R^{\pm})=-(\partial_x R^{\pm})\frac{\partial C^{\pm}}{\partial x}. \tag{26}$$

In the case nonlinearity is large, the right hand side of Eq. (26) needs to be solved by a finite difference. Solving Eqs. (25) and (26) with the CIP method, we obtain the solution with the third order accuracy both in time and space. Taking the average and the difference of the Riemann invariants obtained with the CIP interpolation, we obtain Γ and u (and their derivatives as well) at the new time step t^{n+1}:

$$\Gamma^{n+1}=\frac{1}{2}\left[\Gamma^{+}+\Gamma^{-}+\frac{1}{2}(u^{+}-u^{-})\right], \tag{27}$$

$$\partial_x\Gamma^{n+1}=\frac{1}{2}\left[\partial_x\Gamma^{+}+\partial_x\Gamma^{-}+\frac{1}{2}(\partial_x u^{+}-\partial_x u^{-})\right], \tag{28}$$

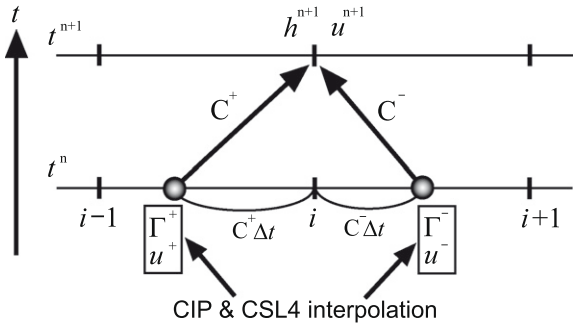

Fig. 3. Schematic of characteristic propagation.

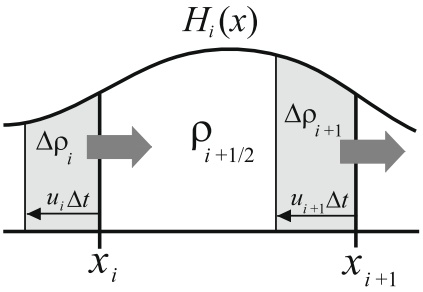

Fig. 4. Schematic of conventional flux.

$$u^{n+1} = \frac{1}{2}[u^+ + u^- + 2(\Gamma^+ - \Gamma^-)], \tag{29}$$

$$\partial_x u^{n+1} = \frac{1}{2}[\partial_x u^+ + \partial_x u^- + 2(\partial_x \Gamma^+ - \partial_x \Gamma^-)]. \tag{30}$$

This CIP method of characteristics (hereafter, we call it the CIP–MOC) was first proposed by Ogata et al. and their result shows high efficiency and accuracy [7]. Although the method does not guarantee the complete mass (height h) conservation, their result shows fairly sufficient conservation of both height and vorticity. However, the conservation becomes critical in applications to nonlinear problems or long-term simulations. In order to overcome these problems, we interpolate $h^\pm$ and $\partial_x h^\pm$ at the upstream departure point with the CSL4 scheme from the values of h^n and $\partial_x h^n$ (instead of Γ^n and $\partial_x \Gamma^n$) which are defined at grid points and obtained by the characteristic method, and are transformed into $\Gamma^\pm$ and $\partial_x \Gamma^\pm$:

$$\Gamma^\pm = \sqrt{g h^\pm_{\mathrm{CSL4}}}, \tag{31}$$

$$\partial_x \Gamma^\pm = \frac{\partial_x h^\pm_{\mathrm{CSL4}}}{2}\sqrt{\frac{g}{h^\pm_{\mathrm{CSL4}}}}, \tag{32}$$

where the subscript CSL4 in variables means that they are interpolated with the CSL4 scheme. Then substituting Eqs. (31) and (32) into Eqs. (27)–(30), the height and its spatial derivative at new time step can be obtained simply by inverse transformations:

$$h_i^{n+1} = \left(\Gamma_i^{n+1}\right)^2/g, \tag{33}$$

$$\partial_x h_i^{n+1} = 2\partial_x \Gamma_i^{n+1}\sqrt{\frac{h_i^{n+1}}{g}}. \tag{34}$$

Since we need the cell mass ρ for the next time step to construct CSL interpolation, we also need to transport ρ in a flux form (for complete conservation) for the next time step.

In the original CIP–CSL scheme, the flux $\Delta\rho$ was calculated as the mass between the point x_i and the upstream departure point $x_d = x_i - \int_t^{t+\Delta t} u_i\,dt$ as follows [17,18,20]:

$$\Delta\rho_i = \int_{x_d}^{x_i} h(x)dx. \tag{35}$$

However, the direct application of this method to the shallow water equations causes oscillation, because the velocity and height field develop together and it is difficult to find the upstream departure point. In an alternative way, the flux $\Delta\rho$ can also be estimated by interpolating the height and the velocity in time at x_i:

$$\Delta\rho_i = \int_t^{t+\Delta t} u(t, x_i)h(t, x_i)dt. \tag{36}$$

While conventional mass advection equation (35) means that the volume between x_i and the upstream departure point x_d shift to the next cell, the present method integrates the mass passing x_i through during Δt. The conventional time-averaged flux for Eq. (36) suggested in some literatures [8,23] uses the flux at time n and the predicted flux at time $n+1$ by the original conservation equation. The easiest choice to interpolate the momentum is linear interpolation because we already have h^{n+1} and u^{n+1}. Using h^{n+1} and u^{n+1}, the momentum at x_i can be linearly interpolated as

$$u(t, x_i)h(t, x_i) = u_i^n h_i^n + \frac{\left(u_i^{n+1}h_i^{n+1} - u_i^n h_i^n\right)}{\Delta t}(t - t^n). \tag{37}$$

However, the trapezoidal integration of this simple linear interpolation during whole Δt has low accuracy and easily makes phase error even with small CFL numbers. In order to enhance the time accuracy of volume flux, we propose to calculate $h^{n+1/2}$ and $u^{n+1/2}$ also with MOC, use the momentum at $t^{n+1/2}$ and the Simpson's rule integration as follows (Fig. 5):

$$\Delta\rho_i = \frac{\Delta t}{6}\left(u_i^n h_i^n + 4u_i^{n+1/2}h_i^{n+1/2} + u_i^{n+1}h_i^{n+1}\right). \tag{38}$$

With this newly obtained $\rho_{i+1/2}^{n+1}$ by Eq. (18), the CSL4 interpolation can be constructed at the next time step, and the whole procedure in one dimension at a time step is completed here.

The reason why we propose the new method for flux estimation here is because the conventional flux estimation equation (35) is not valid for the shallow water equations.

When the conventional method equation (35) is taken, the peak height of a wave keeps rising and soon oscillation occurs in a next example problem. This is because the cell mass is not coupled with height on grid points. Let us think about a still water column (Fig. 6). If the time step interval is largely taken, after the first step, the height on grid points will form two smaller water column propagating to each side by the method of characteristics, however, the cell mass will still be at the initial place because initially the velocity is all zero (no flux is produced). On the other hand, the present method produces flux even in such a case because this method considers the time evolution of velocity on grid points during the time step interval. The present method enables applications of the CIP–CSL scheme to the method of characteristics for the shallow water equations (hereafter, we call it the CSL–MOC).

3.2. Result in almost linear case

We tested the present method in two cases, one is almost a linear case and the other is a nonlinear case such as a shock problem. First, in almost the linear case, the initial profile is given as below:

$$h(x, t=0) = 1.0 + 0.01 \cdot \exp\left\{-\left(\frac{x - X_{max}/2}{5.0}\right)^2\right\}. \tag{39}$$

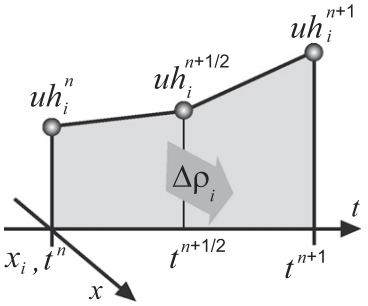

Fig. 5. Schematic of present flux.

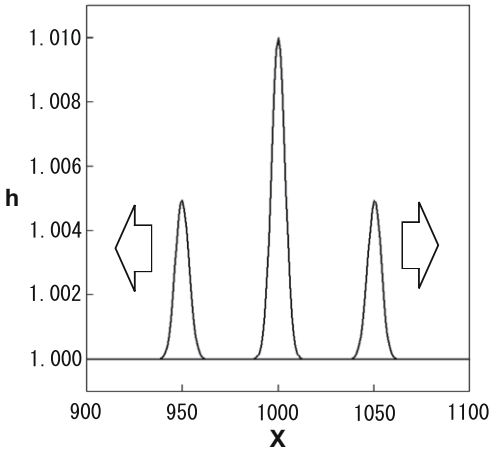

Fig. 6. Initial condition and solution behavior.

Velocity u_i is zero on all points. In this case, as time passes, the initial still water column is split in two and the waves propagate in each direction as shown in Fig. 6. The number of meshes NX is 2000 and the mesh size is $\Delta x = 1.0$. Time is developed until $t = 800$. Since the nonlinearity is very small, the right hand side of Eq. (26) is not solved here. The gravitational acceleration is set to $g = 1$ $(Fr = 1)$ in all one-dimensional calculations.

Fig. 7 shows the wave profiles calculated with the present method (CSL–MOC), the CIP–MOC, and the MOC using the cubic-Lagrange method (hereafter, we call it the CUL–MOC) at $t = 800$ with CFL = 0.4. We define $\mathrm{CFL} \equiv \mathrm{abs}(C^{\pm}_{max}\Delta t)/\Delta x$ throughout this paper. It has been already shown that the CIP–MOC has several advantages comparing with the CUL–MOC of which accuracy strongly depends on the grid size, and here Fig. 7 shows that the present method takes over advantages of the CIP–MOC and besides keeps the peak height of the wave better than the CIP–MOC. It may not seem Fig. 7 shows that the CSL–MOC has such a big advantage comparing with the CIP–MOC, however, the difference becomes obvious in long time integration. The conservation of the present scheme is examined by integrating until $t = 10,000$ and the results are shown in Fig. 8. We estimated the error with the following equation:

$$Error = \left|\sum f_{istep} - \sum f_{initial}\right| \Big/ \sum f_{initial}. \tag{40}$$

In the case of height error, f is substituted with h. Fig. 8 shows that the height conservation is better by the order of 10^5 with the present method than only the CIP method. Note that the cell mass in the whole computational region is completely conserved, because it is transported in the flux form. Since the height error in Fig. 8 is constrained by this completely conserving volume, it is guaranteed not to increase unilaterally.

Fig. 9 shows the difference by CFL numbers. It can be seen that shape and propagation speed of wave are almost the same as each other for different CFL numbers, that is, numerical results do not change very much even if time step interval is largely taken (CFL > 0.7—0.8). This shows that phase error and damping rate of the CSL–MOC for various CFL numbers are very

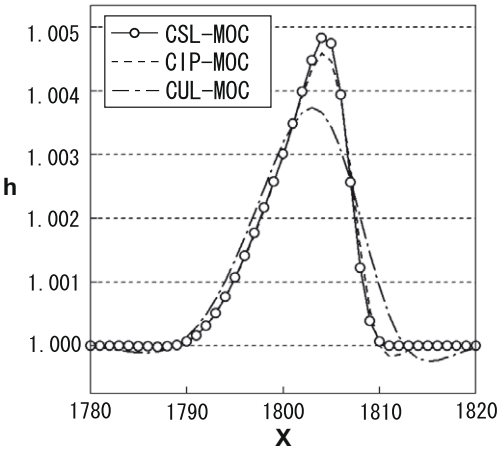

Fig. 7. Difference by scheme.

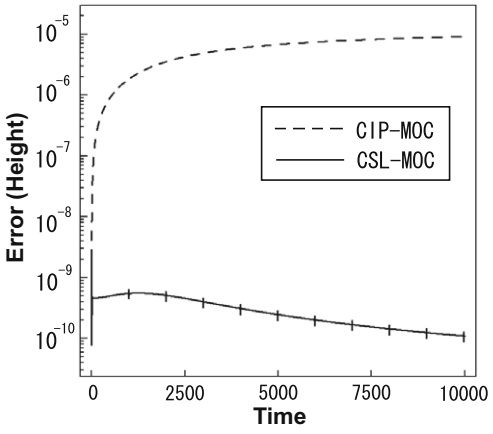

Fig. 8. Height error.

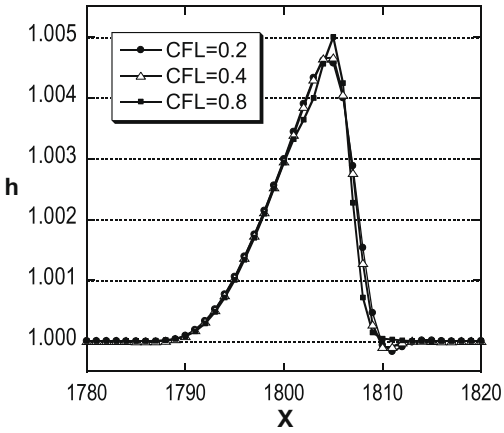

Fig. 9. Difference by CFL.

low. This is also the big advantage for calculations of the gravity waves without dispersion of phase speeds and damping of wave amplitudes.

3.3. Nonlinear case

In particular cases such as shock wave problems, exact solutions are given for the shallow water equations [24]. In these cases, the right hand side of Eq. (26) is solved with finite difference because of the substantial nonlinearity.

3.3.1. Artificial viscosity

Although the present method guarantees mass conservation, since method of characteristics itself is in non-conservative form, shock front gets delayed from the one of exact solutions in dam break problems. Therefore, we introduce an artificial viscosity to enhance the solution in such problems. In solving compressible Euler equations, an artificial viscosity is added in order to enhance the energy conservation and meet with exact solutions [25]. We employed a form similar to the one used in solving compressible flow:

$$q^{\pm} = \begin{cases} \frac{C_v}{g}(\Delta u^{\pm})^2 & \text{if } \Delta u^{\pm} < 0, \\ 0 & \text{otherwise}, \end{cases} \tag{41}$$

where

$$\Delta u^{\pm} = \mathrm{sgn}(C^{\pm})(u_i - u_{i-\mathrm{sgn}(C^{\pm})}), \tag{42}$$

$$\Gamma^{\pm}_{vis} = \sqrt{g(h^{\pm} + q^{\pm})}, \tag{43}$$

and the viscosity coefficient C_v is set to unity. Since the height is already guaranteed to conserve, we replace $\Gamma^{\pm}$ only in Eq. (29) with Eq. (43). Even though the present method gives much closer solution to the exact solution in shock problem without this artificial viscosity compared to the CIP–MOC, it does help to suppress some small oscillation at the shock front. We used 10,000 grid points with maximum CFL $\simeq 0.2$.

3.3.2. Result

The comparison of the CIP method and the present method with the exact solution at $t = 400$ is shown in Fig. 10 and it shows clearly that the present method has an advantage in such a discontinuous case. Fig. 11 shows the long calculation with three times wider domain (30,000 grid points) than Fig. 10. Grid points are depicted every 1000 points for clear comparison. Slight delay of shock front by the CSL–MOC appears at $t = 1200$ (about 2.7% slower than a theoretical value) due to the intrinsic property of characteristics. However, this difference is quite small for practical applications as discussed in [24], and it is very important to capture all features accurately without any numerical instabilities.

However, since such a nonlinear profile is an unlikely circumstance in meteorology, we did not use this artificial viscosity in further examinations.

3.4. Numerical tests for large CFL numbers in one dimension

Next, the CSL–MOC scheme is applied to large CFL numbers. Gravity wave play a minor rule in synoptic-scale calculations, on the other hand, effects of gravity waves cannot be neglected in mesoscale calculations. Even in both cases, fast gravity waves make time step interval Δt strictly bounded in explicit schemes. Therefore, stable and accurate methods which can take large Δt are required for long time calculations [4].

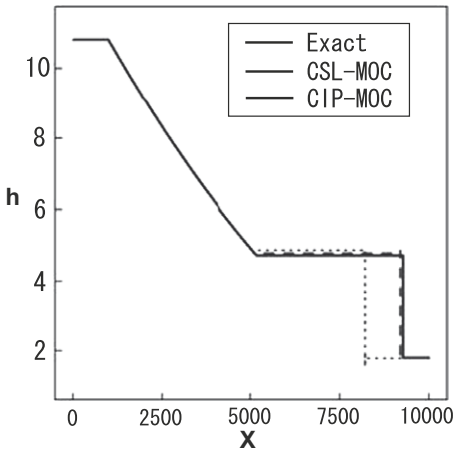

Fig. 10. Comparison of shock between CIP–MOC and CSL–MOC at $t = 400$.

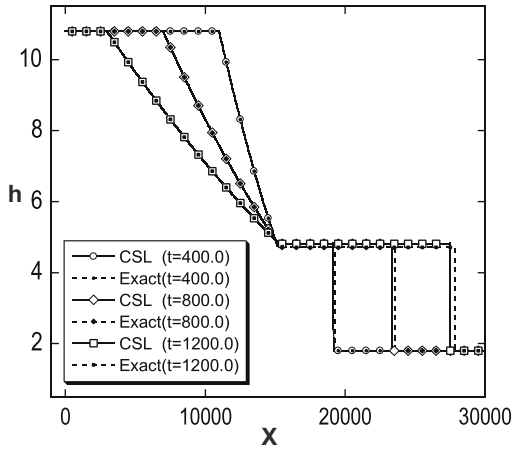

Fig. 11. Shock at $t = 400$, 800, 1200 solved with CSL–MOC.

Some applications of the CIP–MOC to large CFL numbers have already shown that it is unconditionally stable, and its amplitudes and phase speeds of waves are highly accurate even for large CFL numbers [7]. In this section, we shall extend the CSL–MOC to large CFL numbers calculations (Fig. 12).

In semi-Lagrange approaches, since the upstream departure point x_i^p can be easily found by tracing the trajectory across several grid points in Δt even for large CFL numbers as follows:

$$x_i^p = x_i - \int_t^{t+\Delta t} u_i \, dt. \tag{44}$$

The value and spatial derivative used in the CIP or the CIP–CSL4 can be also interpolated at the cell which includes the upstream departure point x_i^p [20,16]. The time evolution of ρ can be also calculated by the mass flux $\Delta\rho$ in Δt [20]. The standard 1/3 Simpson's rule is adopted to calculate $\Delta\rho$ as Eq. (18) for large CFL numbers, and Eq. (38) is changed as

$$\Delta\rho_i = \frac{\Delta t}{3L_{level}}\left[(u_i h_i)^n + 2\sum_{l=1}^{L_{level}/2-1}(u_i h_i)^{n+\frac{2l}{L_{level}}} + 4\sum_{l=1}^{L_{level}/2}(u_i h_i)^{n+\frac{2l-1}{L_{level}}} + (u_i h_i)^{n+1}\right], \tag{45}$$

where L_{level} is the number of substeps in Δt. For example, $L_{level} = 2$ in Eq. (45) corresponds to the case of CFL $\leqslant 1$ Eq. (38), and L_{level} should be an even number for the standard 1/3 Simpson's rule when CFL is larger than unity. In the present scheme, we take $L_{level} = 2 \times (1 + int(\mathrm{CFL}))$.

First, the same initial condition as Eq. (39) is taken as the test problem. The number of meshes is 2000 and the grid interval is $\Delta x = 1.0$. Eqs. (19) and (20) are integrated up to $t = 800.0$ with several CFL numbers.

Fig. 13 shows the result of wave propagations for CFL = 0.4, 4.0, 10.0, 40.0. Numerical solutions are stable, and wave amplitudes and propagation speed are approximately preserved even for large CFL numbers. However, profiles of large

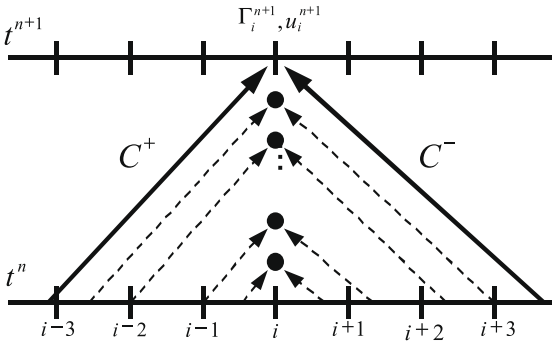

Fig. 12. Schematic of characteristic propagation for large CFL.

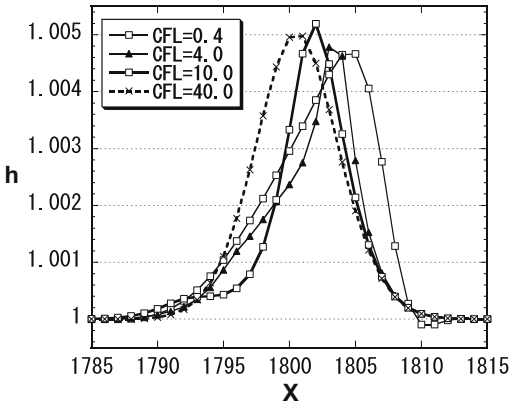

Fig. 13. The height at $t = 800.0$ under the initial condition of Eq. (39) for CFL = 0.4, 4.0, 10.0, 40.0.

CFL numbers deviate from the solution of CFL = 0.4. This is because the wave propagation speed rapidly changes in time and space.

In order to obtain correct solutions, the time step interval Δt must be taken in such a way that $\Delta C \Delta t / \Delta x \sim 1$ (called *Lipschitz condition* [4]) can be satisfied, where ΔC is a change of (characteristic) speeds in Δt. This condition is the common restriction in any large CFL calculations using any numerical schemes.

The breakdown of Lipschitz condition by large ΔC will give incorrect solutions. Nonetheless, in semi-Lagrangian approaches, it has already been proved that correct estimations of characteristic speeds in characteristics can give correct numerical solutions even for large CFL numbers [26,7] when ΔC satisfies Lipschitz condition, in other words, longer time step interval can be taken when flows are smooth. The same can be said of multi-dimensional calculations, which will be demonstrated in Section 4.

In order to confirm the speculation, we take the other two initial conditions:

$$h(x, t = 0) = 1.0 + 0.001 \cdot \exp\left\{-\left(\frac{x - X_{max}/2}{5.0}\right)^2\right\}, \tag{46}$$

$$h(x, t = 0) = 1.0 + 0.01 \cdot \exp\left\{-\left(\frac{x - X_{max}/2}{50.0}\right)^2\right\}. \tag{47}$$

The amplitude of perturbation of Eq. (46) is 10 times smaller than Eq. (39), and the perturbation of Eq. (47) is 10 times wider than Eq. (39). Therefore, these two conditions are closer to linear problems than Eq. (39).

The numerical solutions from CFL = 0.2 to 40.0 for Eqs. (46) and (47) are shown in Figs. 14 and 15, respectively.

Both results show good behavior without dispersion of the phase speed and damping of the amplitude in the wide range of CFL numbers. Especially, CFL numbers of both 0.2 and 40.0 are exactly the same as each other in the wide perturbation equation (47).

Therefore, it is concluded that the present scheme can give stable and accurate solutions for large CFL numbers when changes of characteristic speeds are small for one-time step.

The CSL–MOC as well as the CIP–MOC are stable, and numerical solutions are also similar to each other in not only linear but also nonlinear problems even for very large CFL numbers such as 40.0. For example, the overall phase speed and ampli-

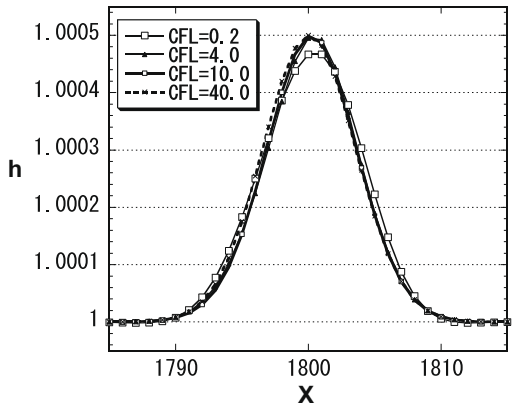

Fig. 14. The height at $t = 800$ under the initial condition of Eq. (46).

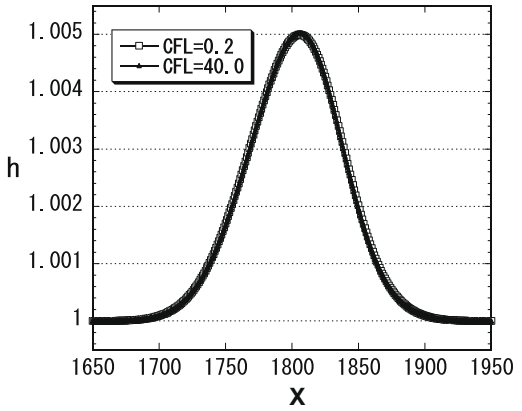

Fig. 15. The height at $t = 800$ under the initial condition of Eq. (47).

tude are maintained very well for very large CFL numbers as well in the CSL–MOC. However, some superiorities of the CIP–CSL4 to the CIP for large CFL numbers are the same as small ones. In conventional implicit solutions without characteristic methods, strong numerical diffusion will make waves smeared out and dispersion error will give incorrect phase speed. As opposed to them, the present method based on semi-Lagrangian approach is able to solve without such disadvantages.

4. Two-dimensional shallow water equations

4.1. Arrangement of height and its integration value in two dimensions

In two dimensions, we employed the same arrangement of conservative quantities (height in present case) as the conventional multi-dimensional CSL as shown in Fig. 16. We define line density in both x-direction $\left(\sigma_x \equiv \int^{\Delta x} h\,dx\right)$ and y-direction $\left(\sigma_y \equiv \int^{\Delta y} h\,dy\right)$ between grid points and cell mass $\left(\rho \equiv \int^{\Delta y}\int^{\Delta x} h\,dx\,dy\right)$ in the middle of 4 grid points. In this arrangement, we

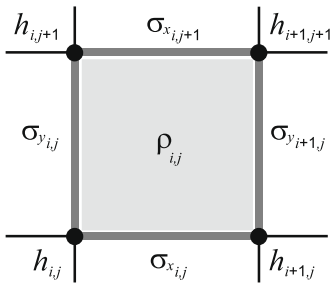

Fig. 16. Arrangement of height and its integration values.

can construct CSL2 and CSL4 interpolation in both the x- and y-directions, so the same procedure as one dimension can be directly implemented in both the x- and y-directions.

4.2. Characteristic formulation

Two-dimensional primitive shallow water equations without effects of bottom topography are written in vector–matrix form as

$$\frac{\partial}{\partial t}\begin{pmatrix} h \\ u \\ v \end{pmatrix} + \begin{pmatrix} u & h & 0 \\ g & u & 0 \\ 0 & 0 & u \end{pmatrix}\frac{\partial}{\partial x}\begin{pmatrix} h \\ u \\ v \end{pmatrix} + \begin{pmatrix} v & 0 & h \\ 0 & v & 0 \\ g & 0 & v \end{pmatrix}\frac{\partial}{\partial y}\begin{pmatrix} h \\ u \\ v \end{pmatrix} + \begin{pmatrix} 0 \\ -fv \\ fu \end{pmatrix} \equiv \frac{\partial \mathbf{W}}{\partial t} + \mathbf{A}(\mathbf{W})\frac{\partial \mathbf{W}}{\partial x} + \mathbf{B}(\mathbf{W})\frac{\partial \mathbf{W}}{\partial y} + \mathbf{F} = \mathbf{0}, \quad (48)$$

where f represents the constant Coriolis parameter.

If let f_0 be the characteristic Coriolis parameter, we can use Eq. (48) as nondimensional equation with the definition in Section 3.1, and the corresponding Rossby number $Ro \equiv U_0/f_0L_0$ is also defined as $f \equiv 1/Ro$ in Eq. (48).

Here, using a directional splitting technique, Eq. (48) is split into two sequential phases. The Coriolis force term is also divided in half and added to each directional phase:

$$\frac{\partial \mathbf{W}}{\partial t} + \mathbf{A}\frac{\partial \mathbf{W}}{\partial x} + \frac{1}{2}\mathbf{F} = \mathbf{0} \quad \mathbf{W} \to \mathbf{W}^*, \quad (49)$$

$$\frac{\partial \mathbf{W}}{\partial t} + \mathbf{B}\frac{\partial \mathbf{W}}{\partial y} + \frac{1}{2}\mathbf{F} = \mathbf{0} \quad \mathbf{W}^* \to \mathbf{W}^{n+1}. \quad (50)$$

Since matrices $\mathbf{A}$ and $\mathbf{B}$ are not commutative, we solve these directional phases in rotation as below in order to maintain second order accuracy in time:

$$\mathbf{W}^{n+2} = L_xL_yL_yL_x\mathbf{W}^n, \quad (51)$$

where L_x and L_y represent the operation of Eqs. (49) and (50), respectively [27,28].

Since there is no difference between the x-directional operation and the y-directional operation, we will mainly demonstrate the operation procedure in the x-direction. In the exact same way as one dimension, we can find the eigenvalues of matrix $\mathbf{A}$ with $\mathbf{L}$ and $\mathbf{L}^{-1}$:

$$\mathbf{L}^{-1}\frac{\partial \mathbf{W}}{\partial t} + (\mathbf{L}^{-1}\mathbf{A}\mathbf{L})\mathbf{L}^{-1}\frac{\partial \mathbf{W}}{\partial x} + \mathbf{L}^{-1}\frac{1}{2}\mathbf{F} = \mathbf{L}^{-1}\frac{\partial \mathbf{W}}{\partial t} + \begin{pmatrix} C_x^+ & 0 & 0 \\ 0 & C_x^- & 0 \\ 0 & 0 & u \end{pmatrix}\mathbf{L}^{-1}\frac{\partial \mathbf{W}}{\partial x} + \mathbf{L}^{-1}\frac{1}{2}\mathbf{F} = 0, \quad (52)$$

where

$$C_x^{\pm} = u \pm \Gamma, \quad (53)$$

$$\mathbf{L} = \begin{pmatrix} 1 & 1 & 0 \\ \sqrt{gh} & -\sqrt{gh} & 0 \\ 0 & 0 & 1 \end{pmatrix}, \quad \mathbf{L}^{-1} = \begin{pmatrix} 1 & \sqrt{h/g} & 0 \\ 1 & -\sqrt{h/g} & 0 \\ 0 & 0 & 1 \end{pmatrix}. \quad (54)$$

Decomposing Eq. (52) leads to the following three equations,

$$\frac{\partial R_x^{\pm}}{\partial t} + C_x^{\pm}\frac{\partial R_x^{\pm}}{\partial x} \mp \frac{1}{4}fv = 0, \quad (55)$$

$$\frac{\partial v}{\partial t} + u\frac{\partial v}{\partial x} + \frac{1}{2}fu = 0, \quad (56)$$

where $R_x^{\pm} = \Gamma \pm u/2$ are the Riemann invariants. What these three equations mean is that two Riemann invariants $R_x^{\pm}$ and v propagate with the characteristic speeds of $C_x^{\pm}$ and u (Fig. 17), respectively, and the Coriolis force (the third term) is added to each Riemann invariant along each characteristic line. Based on this consideration, we discretized the Riemann invariants and v as follows (see Fig. 18):

$$R_x^{\pm} = \Gamma^{\pm} \pm \frac{1}{2}u^{\pm} \mp \frac{1}{4}f\Delta t\frac{(v^{\pm} + v^*)}{2}, \quad (57)$$

$$v^* = v^0 + \frac{1}{2}f\Delta t\frac{(u^0 + u^*)}{2}. \quad (58)$$

The Coriolis force term is discretized with the Crank–Nicholson method using the velocity at characteristics foot and at the new time step. Eqs. (57) and (58) are a kind of semi-implicit formulations. However, unlike typical semi-implicit schemes, Eqs. (57) and (58) can be solved explicitly without solving any matrices, and careful choice of a reference geopotential to stabilize numerical schemes is not needed.

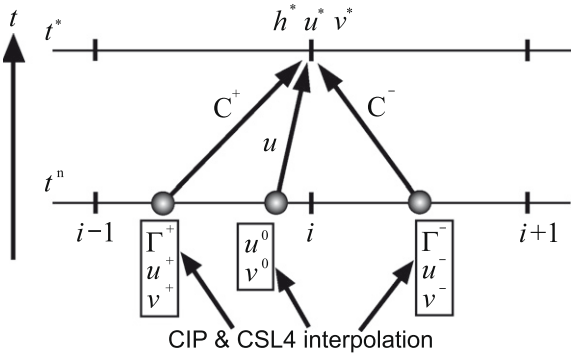

Fig. 17. Schematic of characteristic propagation.

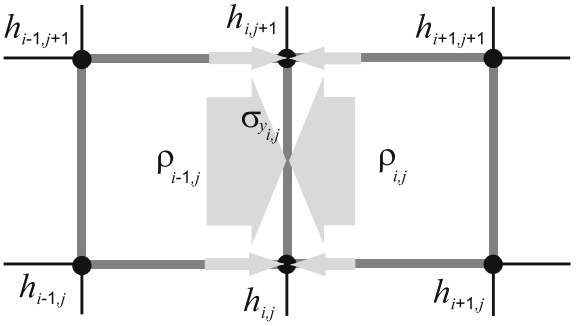

Fig. 18. Schematic of average characteristics propagation.

Using Eq. (58) to Eq. (57), we can explicitly solve Γ^* and u^*, and simply substituting u^* into Eq. (58) for v^*, we obtain all variables on grid points at the new time step t^*.

Formulations for spatial derivatives in both the x- and y-directions are exactly the same as Eqs. (57) and (58), and linear interpolation is used in interpolating spatial derivatives in the y-direction, which we call the M-type CIP method [29]. The same mass advection procedure as in one dimension is applied here to σ_x (which corresponds to $\Delta\rho$ in Eq. (38)), and $\Delta\sigma_x$ is calculated with newly obtained h^* and u^*.

In two dimensions, σ_y and ρ also need to be updated. Here, we propose to take average characteristics between y_j and y_{j+1}. We introduce average values between y_j and y_{j+1} as

$$\bar{h}_{i,j} = \sigma_{y_{i,j}}/\Delta y, \quad \bar{\sigma}_{x_{i,j}} = \rho_{i,j}/\Delta y, \tag{59}$$

$$\bar{u}_{i,j} = (u_{i,j} + u_{i,j+1})/2, \quad \partial_x \bar{u}_{i,j} = (\partial_x u_{i,j} + \partial_x u_{i,j+1})/2, \tag{60}$$

$$\bar{v}_{i,j} = (v_{i,j} + v_{i,j+1})/2 \quad \text{and} \quad \partial_x \bar{v}_{i,j} = (\partial_x v_{i,j} + \partial_x v_{i,j+1})/2. \tag{61}$$

With these averaged values, propagations of average characteristics in the exactly same manner as in one dimension can be implemented. We can construct CSL2 interpolation with $\bar{h}$ and $\bar{\sigma}_x$, and CIP interpolation with $\bar{u}(\bar{v})$ and $\partial_x \bar{u}(\partial_x \bar{v})$. By transforming the $\bar{h}^{\pm}_{\mathrm{CSL2}}$ into $\overline{\Gamma}^{\pm}$ with Eq. (31) and taking the average of Riemann invariants, we obtain $\overline{\Gamma}^*$. Transforming $\overline{\Gamma}^*$ back to the height and multiplying Δy, the y-direction line density σ^*_y at new time step is obtained. This procedure corresponds to tracking the average characteristics between y_j and y_{j+1}.

The remaining ρ is updated with a similar method to σ_x. The x-direction flux $\Delta\rho_x$ between y_j and y_{j+1} in the phase of Eq. (49) can be estimated as follows:

$$\Delta\rho_{x_{i,j}} = \frac{1}{6}\left(\bar{u}\sigma^n_{y_{i,j}} + 4\bar{u}\sigma^{\frac{n+*-n}{2}}_{y_{i,j}} + \bar{u}\sigma^*_{y_{i,j}}\right)\Delta t, \tag{62}$$

where $\bar{u}\sigma^n_{y_{i,j}} = \bar{u}^n_{i,j}\sigma^n_{y_{i,j}}$. All procedure in Eq. (49) is completed here. All procedure in x-direction can be directly adopted by simply exchanging the interpolation direction, velocity in the other (y-) direction. Detailed discussions of multi-dimensional CIP–CSL schemes in views of numerical tests can be also referred to previous literatures [19,20].

4.3. Numerical results

First, we tested the present method with almost linear condition by giving a small perturbation and the initial height profile is given by

$$h(x,y,t=0) = 1.0 + 0.01 \cdot \exp\left\{-\left(\frac{x - X_{max}/2}{5.0}\right)^2 - \left(\frac{y - Y_{max}/2}{5.0}\right)^2\right\}. \tag{63}$$

The perturbation is so small that the characteristic speed is almost 1.0 everywhere in this problem. The grid interval is set to $\Delta x = \Delta y = 1.0$ and the number of grid points is 200 in both x- and y-directions. The gravitational acceleration is set to $g = 1$ ($Fr = 1$) and the Coriolis parameter $f = 0$. Velocity is set zero on all points. We examined the difference by CFL up to 0.4 since phase error becomes significant with CFL > 0.7—0.8 as shown in one dimension case.

Fig. 19 shows that the position of the wave exactly matches with the ones calculated by the CIP–MOC even with CFL $= 0.4$, which means that both point values and cell mass are transported in correct velocity in two dimensions. The cross-section profile at $t = 60.0$ is shown in Fig. 20 and the height contour is shown in Fig. 21. They show that the effect of directional splitting does not show up yet with CFL $= 0.4$. Furthermore the conservation is complete while the conservation of the CIP–MOC keeps deteriorating as time proceeds (Fig. 22).

The two-dimensional CSL–MOC scheme can be also extended to large CFL numbers using the formulation of one dimension. As for x-direction for instance, the characteristics equations (57) and (58) with the upstream departure point equation (44) can be used for two sets (h, u, v) and $(\bar{h}, \bar{u}, \bar{v})$, and the flux equation (45) for $(\Delta\sigma_x, \Delta\rho_x)$. The similar procedure can be implemented in the y-direction.

Shown in Figs. 23 and 24 are height contours and cross-sections for each CFL number at $t = 60.0$. The initial condition, the grid interval and the number of grid points are the same as calculation of Eq. (63) with the small CFL number (=0.4).

Although the contour of CFL = 1.5 seems to be almost the same as CFL = 0.4, the cross-sections of the x- and y-directions are a little bit different from the diagonal profile. As shown in the previous literature of the CIP–MOC method [7], the CSL–MOC scheme also produces incorrect results as CFL numbers become larger and Lipschitz condition is broken, as discussed in Section 3.4.

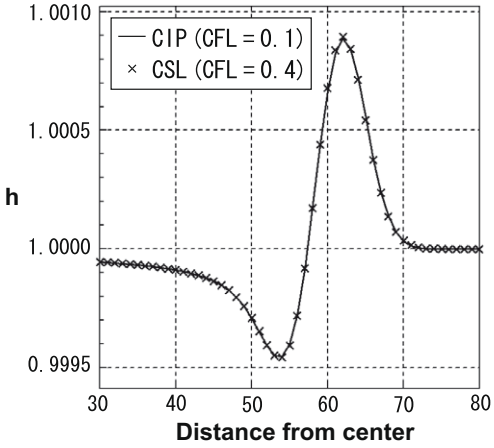

Fig. 19. Cross-section comparison with CIP–MOC.

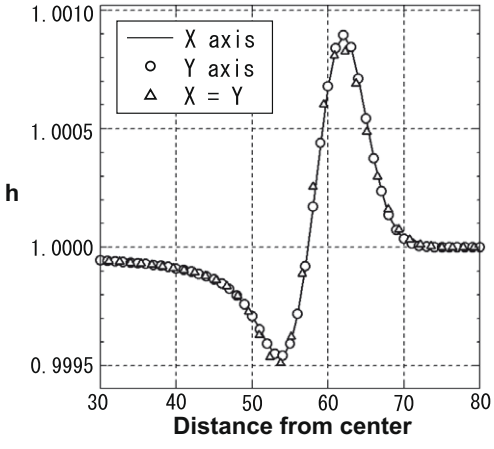

Fig. 20. Cross-section of CSL–MOC at $t = 60.0$.

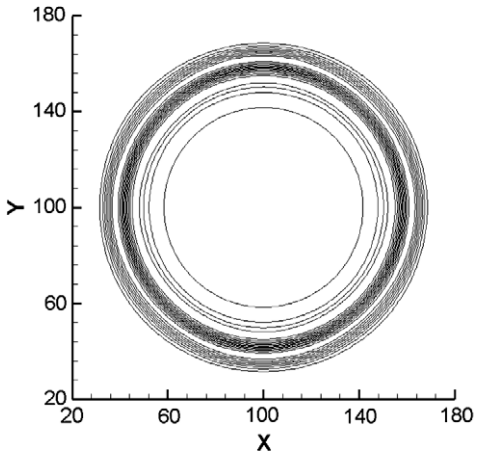

Fig. 21. Height contour at $t = 60.0$ (CFL = 0.4).

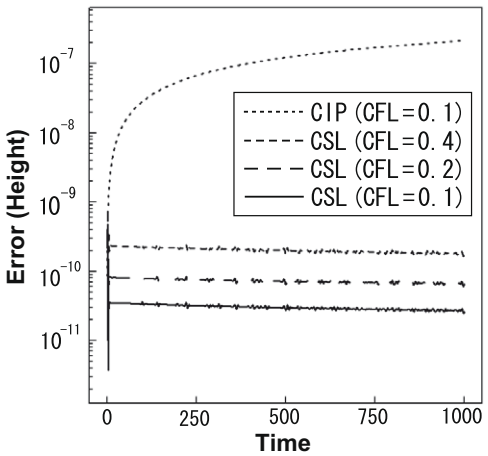

Fig. 22. Height conservation comparison.

For comparison, an example closer to linear problem than Eq. (63) is examined by setting the amplitude of initial height h to 0.001 and the width of initial distribution to 50.0:

$$h(x,y,t=0) = 1.0 + 0.001 \cdot \exp\left\{-\left(\frac{x - X_{max}/2}{50.0}\right)^2 - \left(\frac{y - Y_{max}/2}{50.0}\right)^2\right\}. \tag{64}$$

Grid intervals Δx and Δy are also set to 1.0, but the number of grid points is 400 in both x- and y-directions.

Figs. 25 and 26 show height contours and cross-sections, and Fig. 27 displays cross-sections near the top of wave for each CFL number at $t = 96.0$.

It can be seen that the profile of CFL = 8.0 is almost a circle and effects of fractional steps hardly appear. However, the profile of CFL = 12.0 slightly deviates from a circle and the inside of the profile of CFL = 16.0 becomes a square shape. The difference can be clearly seen in Fig. 27.

Since the initial height of Eq. (64) is 10 times smaller and the width is 10 times larger than Eq. (63), the change of the speed of gravity waves $\left(\sim \Delta\left(\sqrt{gh}\right)\right)$ is about 10 times smaller. Therefore, the adequate CFL number of Eq. (64) under Lipschitz condition is roughly estimated to be ~8.0.

The detailed discussion of merits and demerits of fractional techniques with the CIP/CIP–CSL schemes for large CFL numbers has already been given [20,7]. Notice that what is important in semi-Lagrange approaches is whether stable and robust solutions can be obtained and typical features of numerical solutions are not lost even for large CFL numbers, and correct solutions can be obtained under Lipschitz condition. For example, complete nonlinear problems such as shock wave problems should be solved in CFL < 1 and semi-Lagrange approaches for large CFL numbers cannot be applied. However, they can be very effective approaches for calculations of not only fast waves such as gravity waves but also fast flows with small

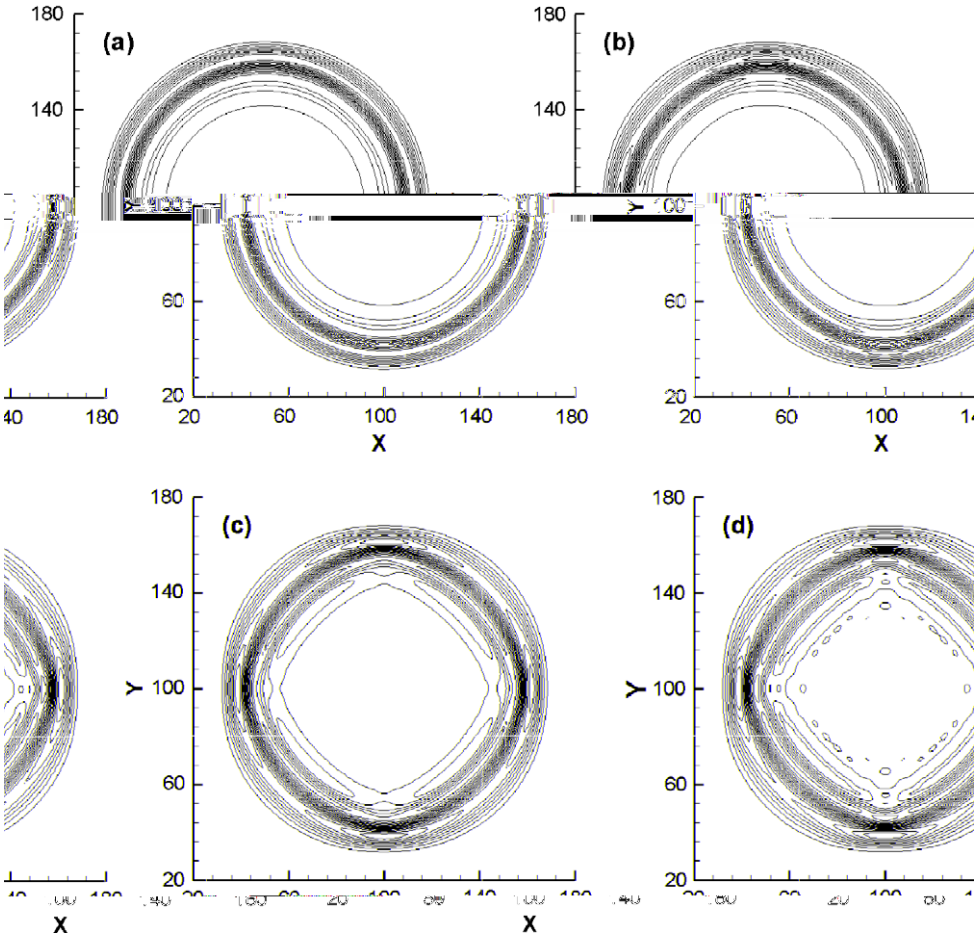

Fig. 23. The comparison of height contours among several CFL numbers at $t = 60.0$. The initial height is Eq. (63). (a) CFL = 0.4; (b) CFL = 1.5; (c) CFL = 2.0; (d) CFL = 2.5.

changes such as jet-stream. Some results of large CFL numbers shown have indicated that the present CSL–MOC scheme has above-mentioned important merits and possibilities for such variety of fields.

4.4. The effect of Coriolis force

Next, we tested the same example as the previous section but with the presence of the Coriolis force. The Coriolis parameter is set to $f = 1.0$ ($Ro = 1$). In this case, the pressure (height) gradient gradually balances with the Coriolis force and generate geostrophic wind. The initial profile is given by

$$h(x,y,t=0) = 1.0 + 0.01 \cdot \exp\left\{-\left(\frac{x - X_{max}/2}{10.0}\right)^2 - \left(\frac{y - Y_{max}/2}{10.0}\right)^2\right\}. \tag{65}$$

All the other condition is the same as the previous example. In two dimensions with the Coriolis force, there are two quantities which are also conserved other than the height [1]. They are defined as

$$\eta \equiv f + \zeta \quad \text{and} \quad P \equiv \frac{\eta^2}{2h}, \tag{66}$$

and termed the absolute vorticity and the (absolute) potential enstrophy respectively, where $\zeta = \mathbf{k} \cdot \nabla \times \mathbf{u}$ is the vorticity of z-component and $\mathbf{k}$ is the unit vector in the z-direction. Here, we examined not only the conservation of height but also the conservation of η and P. The same as height, the errors of η and P are estimated with Eq. (40) by substituting η or P into f.

Fig. 28 shows the time development of height contour, velocity field and absolute vorticity contour until $t = 1000$. The water column is influenced by periodic boundary condition because the wave which propagates away comes back from the other side, especially after $t = 500$. Even with this disturbance, the shape of water column is kept with good symmetry at $t = 1000$.

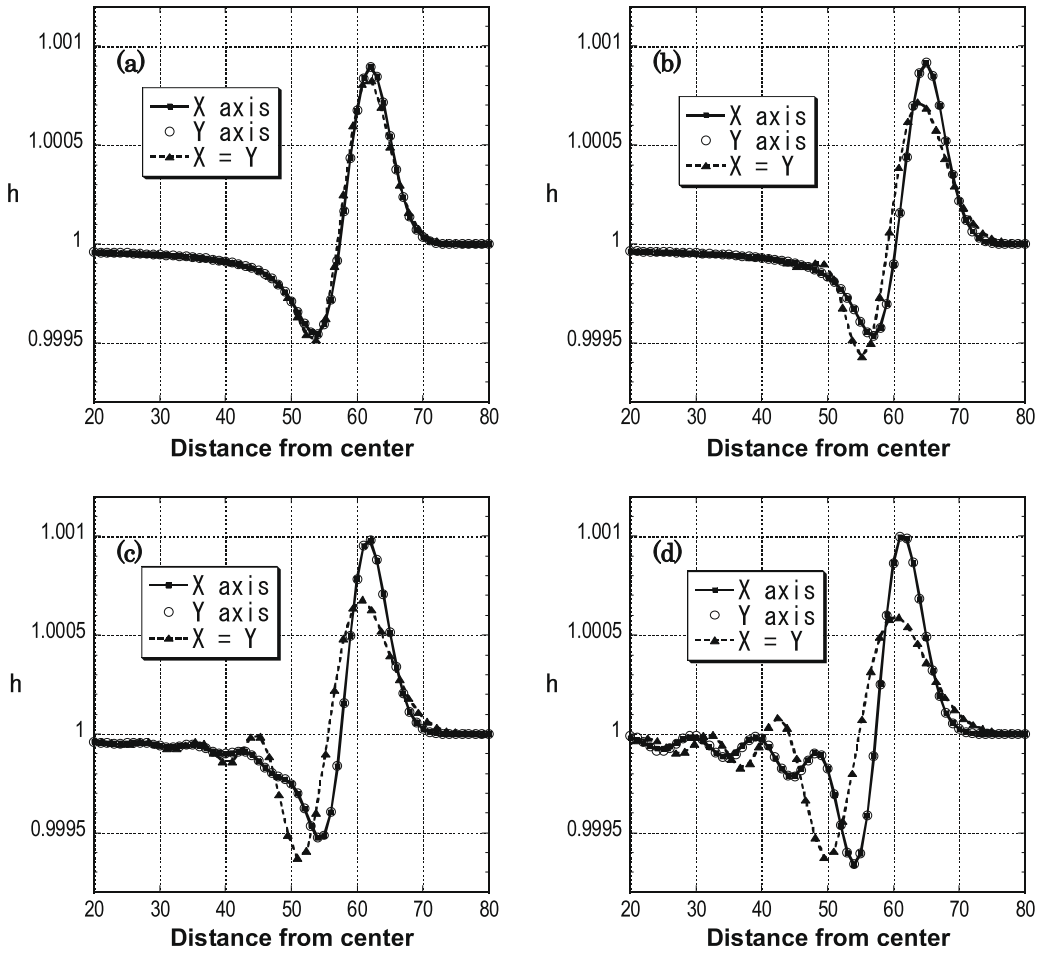

Fig. 24. The comparison of height cross-sections for each CFL number at $t = 60.0$ in Eq. (63). (a) CFL = 0.4; (b) CFL = 1.5; (c) CFL = 2.0; (d) CFL = 2.5.

The height is conserved with almost the same order as in one dimension as shown in Fig. 29(a). Note that the total mass (integral of height, summation of ρ) in the computational region is completely conserved as in one dimension. In two dimensions with the Coriolis force, the absolute vorticity and the potential enstrophy are also conserved in addition to the height very well compared with the CIP–MOC, and all errors of the CSL–MOC do not increase as time goes on (Fig. 29(b) and (c)).

Last of all, we applied the present scheme to an unstable zonal jet problem [30,7]. In this example, zonal potential vorticity is initially set with Eq. (67) in a perturbed coordinate defined by Eq. (68):

$$q(x,y,t=0) = \begin{cases} 4\pi(1.0 + \mathrm{sgn}(\tilde{y})(0.5 - ||\tilde{y}| - 0.5|)) & \text{if } |\tilde{y}| < 1.0, \\ 4\pi & \text{otherwise}, \end{cases} \tag{67}$$

$$\tilde{y} = y + C_m \sin(mx) + C_n \sin(nx). \tag{68}$$

Perturbation parameters are set to $C_m = -0.1,\ C_n = 0.1,\ m = 2$ and $n = 3$, respectively. The computational region is set to $(0 \leqslant x \leqslant 2\pi,\ 0 \leqslant y \leqslant 2\pi)$. Substituting the geostrophic approximation and $v = 0$ into the definition of potential vorticity and integrating in y-direction numerically, the initial height and velocity are set. The gravitational acceleration and the Coriolis parameter are set to $g = 4\pi^2$ $(Fr = 1/2\pi)$ and $f = 4\pi$ $(Ro = 1/4\pi)$, respectively. The initial condition is so unstable that the vorticity soon split into some vortices. We compared the CSL–MOC with the CIP–MOC in various CFL numbers ($\approx$0.1, 0.2 and 0.4). The number of grid points is 100 in both x- and y-directions.

The potential vorticity contour at $t = 2\pi$ is shown in Fig. 30 and it shows that the flow is transported and developed correctly even in such a strongly nonlinear velocity field. In the same way as former problems, the height conservation is guaranteed by the completely conserving integral of height (Fig. 31). However, the conservations of absolute vorticity and potential enstrophy seem to be a little bit worse than the CIP–MOC. They are expected to be improved by tracking the upstream departure point of Riemann invariants more accurately, or estimating the flux with a better function in Eq. (37).

We also varied the grid size in solving zonal jet and the potential vorticity contours at $t = 2\pi$ are shown in Fig. 32. It shows that fine nonlinear details become observable with higher resolution and steep gradients in vortices are fairly vis-

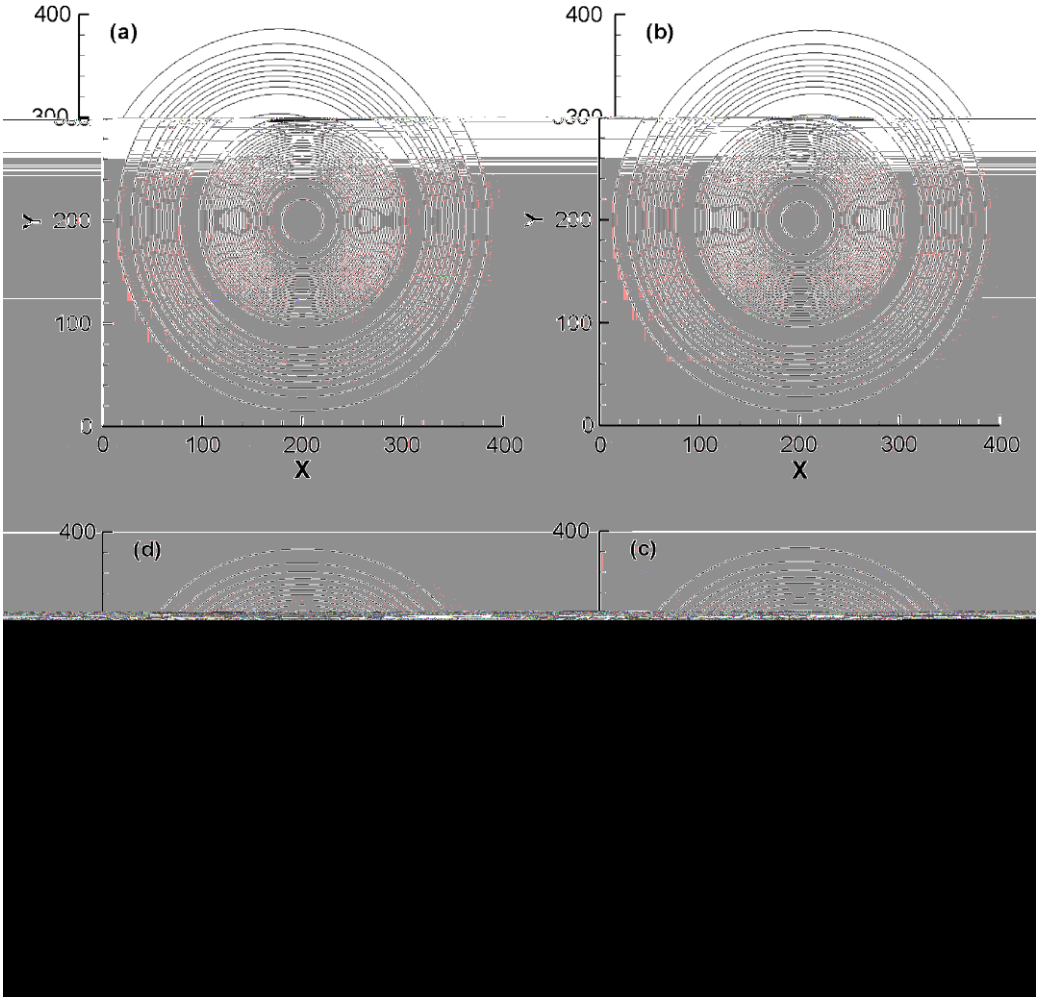

Fig. 25. The comparison of height contours for each CFL number at $t = 96.0$. The initial height is Eq. (64). (a) CFL = 0.4; (b) CFL = 8.0; (c) CFL = 12.0; (d) CFL = 16.0.

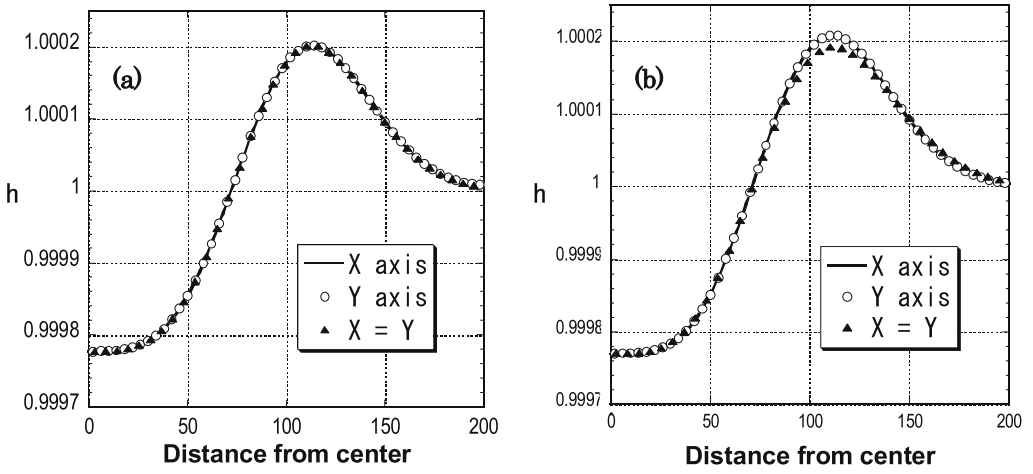

Fig. 26. The comparison of cross-sections between small and large CFL numbers at $t = 96.0$. (a) CFL = 0.4 and (b) CFL = 16.0.

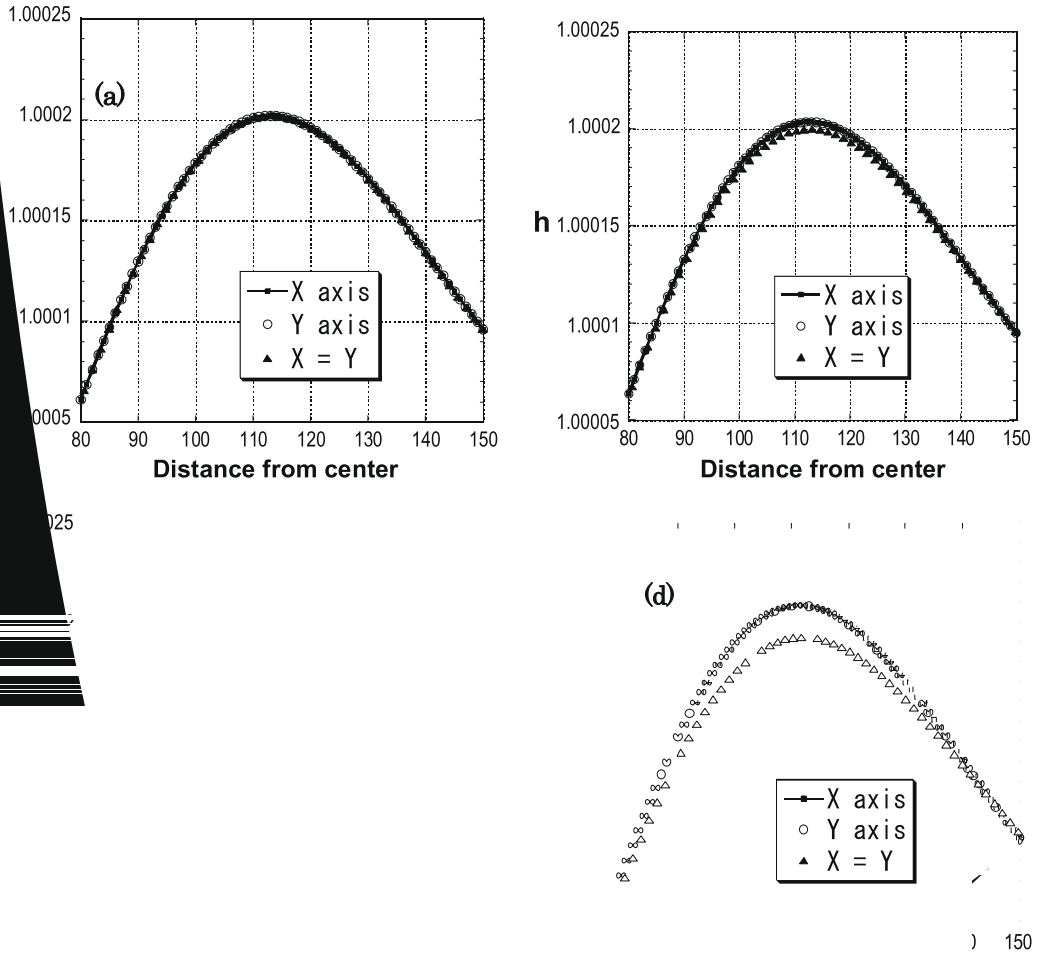

Fig. 27. The comparison of cross-sections near the top of wave in Fig. 26. (a) CFL = 0.4; (b) CFL = 8.0; (c) CFL = 12.0; (d) CFL = 16.0.

s still kept with
finement tech-
ıe graph shows
ion, the present
ı higher resolu-

ng CSL interpo-
s an integral of
ell mass can be
e than the CIP–
on of height on
the other con-
in height con-
hod. The most
h to be applied
en for large CFL

erical geometry

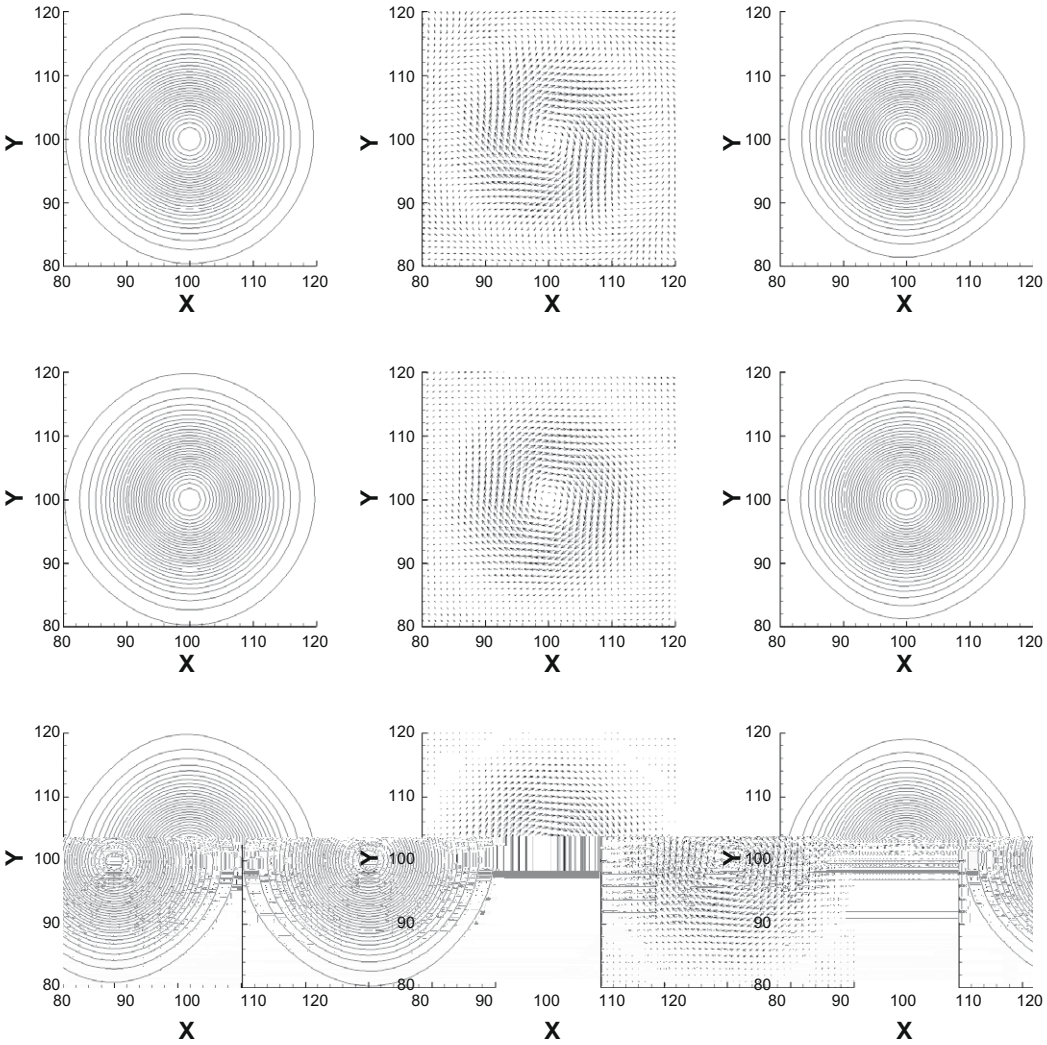

Fig. 28. The height contour (left column), the velocity field (middle column) and the potential enstrophy contour (right column) at $t = 100$ (upper row), $t = 200$ (middle row) and $t = 400$ (lower row).

Although the simplest approach to the spherical geometry is to use the spherical coordinate, singularities close to the poles in the governing equations appear. Some sophisticated techniques have been proposed such as cubed-sphere grid methods in order to resolve this issue [31,32].

As opposed to them, one of the authors brought forward the new adaptive grid system called Soroban-grid [26], which has already been used for various fields such as hydrodynamics. Although it is thought that Soroban-grid is applicable to the spherical geometry as well, the Soroban-grid formulation for the sphere like the whole earth is now under investigation and practical applications will be next future works.

Appendix. CSL–MOC for bottom topography

When the effect of the bottom topography is included, Eq. (48) without the Coriolis force is changed as

$$\frac{\partial \mathbf{W}}{\partial t} + \mathbf{A}(\mathbf{W})\frac{\partial \mathbf{W}}{\partial x} + \mathbf{B}(\mathbf{W})\frac{\partial \mathbf{W}}{\partial y} = \mathbf{S}, \tag{69}$$

where $\mathbf{S}$ is the source term

$$\mathbf{S} = \begin{pmatrix} 0 \\ -g\frac{\partial z}{\partial x} \\ -g\frac{\partial z}{\partial y} \end{pmatrix} \tag{70}$$

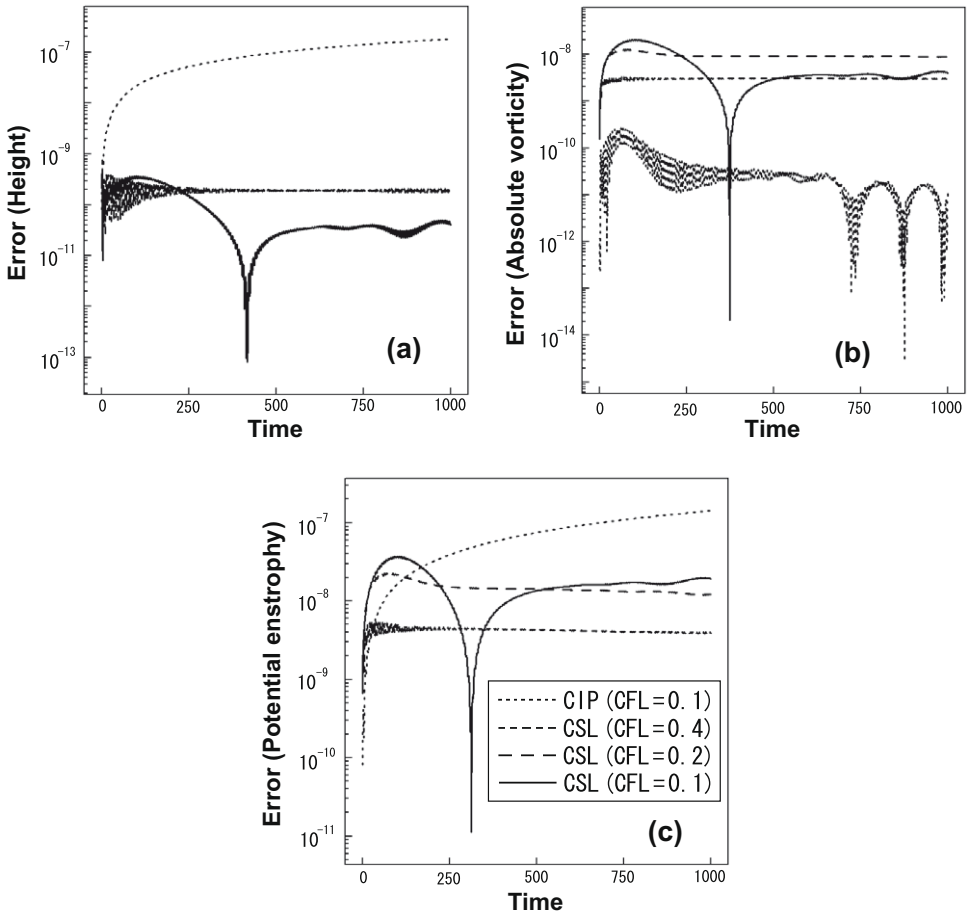

Fig. 29. Conservation error of (a) height, (b) absolute vorticity and (c) potential enstrophy in almost linear problem.

and $z(x,y)$ represents the bottom topography. For example, the one-dimensional shallow water equations are given by

$$\frac{\partial h}{\partial t}+\frac{\partial (uh)}{\partial x}=0, \tag{71}$$

$$\frac{\partial u}{\partial t}+u\frac{\partial u}{\partial x}+g\frac{\partial h}{\partial x}=-g\frac{\partial z}{\partial x}. \tag{72}$$

First, let us consider the most fundamental balance in Eqs. (71) and (72):

$$u(x,t)=0, \quad H(x,t)\equiv h(x,t)+z(x)=H_c(const), \tag{73}$$

where $H(x,t)$ is the water level. Numerical solutions must also remain stationary states, and the following hydrostatic balance must be satisfied on a discretized level in this case [33]:

$$\frac{\partial}{\partial x}\left(\frac{gh^2}{2}\right)+g\frac{\partial z}{\partial x}=0. \tag{74}$$

However, if numerical schemes using water depth h as the primitive variable do not preserve the balance between the depth gradient and the bottom effect in Eq. (74), the real solution equation (73) is violated and spurious oscillations occur. The same can be said of the original CSL–MOC scheme, although it guarantees the complete mass conservation in views of $\rho=\int h\,dx$. In order to solve this problem, the surface gradient method [34] is used for the CSL–MOC scheme. Eqs. (71) and (72) can be changed into the following equations using the water level H instead of the water depth h:

$$\frac{\partial H}{\partial t}+\frac{\partial (uH)}{\partial x}=\frac{\partial (uz)}{\partial x}, \tag{75}$$

$$\frac{\partial u}{\partial t}+u\frac{\partial u}{\partial x}+g\frac{\partial H}{\partial x}=0. \tag{76}$$

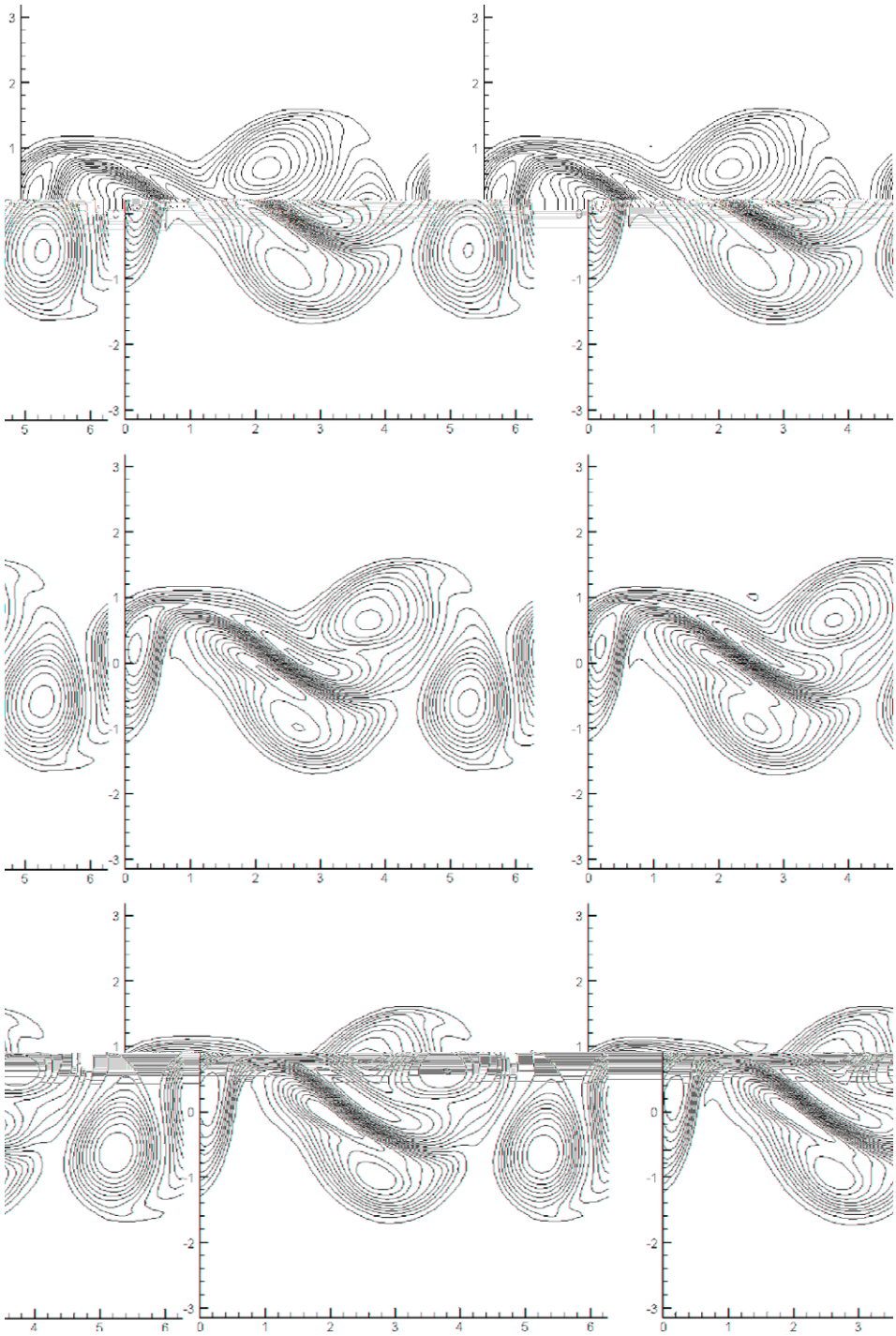

Fig. 30. Potential vorticity contour at $t = 2\pi$ with CIP–MOC (left column) and CSL–MOC (right column) in CFL of 0.1 (upper row), 0.2 (middle row) and 0.4 (lower row).

Then, new characteristics equations can be derived as follows:

$$\frac{\partial R^{\pm}}{\partial t} + C^{\pm}\frac{\partial R^{\pm}}{\partial x} = \frac{g}{2\Gamma_H}\frac{\partial (uz)}{\partial x}, \tag{77}$$

which lead to

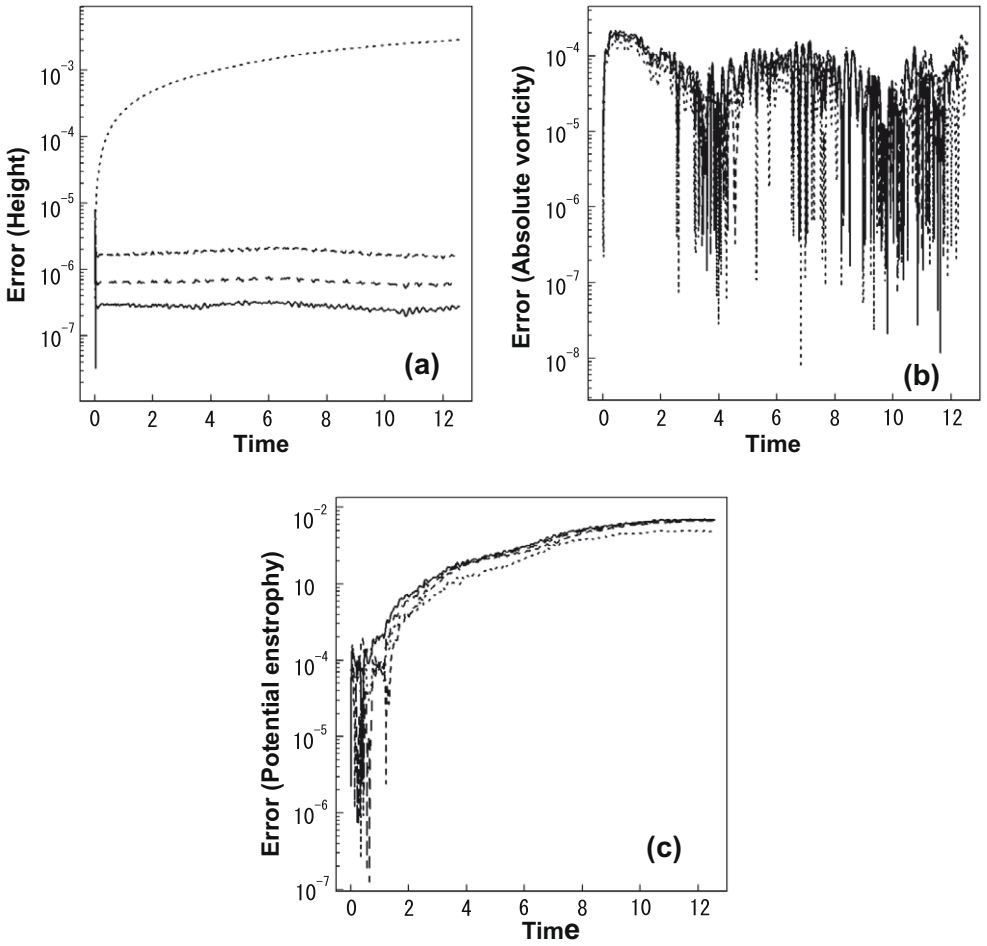

$$R^{n+1} \pm R^{\pm} = \frac{g}{2}\int_0^{\Delta t} \frac{1}{\Gamma_H}\frac{\partial(uz)}{\partial x}\, d\tau^{\pm} \tag{78}$$

where $\Gamma_H \equiv \sqrt{gH}$ and $R^{\pm} \equiv \Gamma_H \pm u/2$, and $\int d\tau^{\pm}$ means time integrations along two characteristics $dx^{\pm}/d\tau^{\pm} = u \pm \Gamma_H$. Therefore, Γ_H and u at next time step can be evaluated as follows (see Fig. 3):

$$\Gamma_H^{n+1} = \frac{1}{2}\left[\Gamma_H^{+} + \Gamma_H^{-} + \frac{1}{2}(u^{+} - u^{-}) + \frac{g}{2}\left(\int_0^{\Delta t} \frac{1}{\Gamma_H}\frac{\partial(uz)}{\partial x}\, d\tau^{+} + \int_0^{\Delta t} \frac{1}{\Gamma_H}\frac{\partial(uz)}{\partial x}\, d\tau^{-}\right)\right], \tag{79}$$

$$u^{n+1} = \frac{1}{2}\left[u^{+} + u^{-} + 2(\Gamma_H^{+} - \Gamma_H^{-}) + g\left(\int_0^{\Delta t} \frac{1}{\Gamma_H}\frac{\partial(uz)}{\partial x}\, d\tau^{+} - \int_0^{\Delta t} \frac{1}{\Gamma_H}\frac{\partial(uz)}{\partial x}\, d\tau^{-}\right)\right]. \tag{80}$$

Time integrations in Eqs. (79) and (80) can be approximated using $dx^{\pm}/d\tau^{\pm} = u \pm \Gamma_H$ as follows [15]:

$$\int_0^{\Delta t} \frac{1}{\Gamma_H}\frac{\partial(uz)}{\partial x}\, d\tau^{\pm} \approx -\frac{(uz)^{\pm} - (uz)^{n}}{\Gamma_H^{\pm}(u \pm \Gamma_H)^{\pm}}. \tag{81}$$

In order to solve Eqs. (79) and (80), we construct the quartic polynomial of H as Eq. (10) in the CIP–CSL4 scheme. The new defined cell volume $P(x,t) \equiv \int H(x,t)dx = \int\{h(x,t) + z(x)\}dx$ at the center of cell between i and $i+1$ grid points can be expressed using the cell mass ρ_i and the bottom topography $z(x)$ located on the grid point

$$P_i = \int_{x_i}^{x_{i+1}} H_i(x)dx = \rho_i + \frac{\Delta x}{2}(z_i + z_{i+1}). \tag{82}$$

Although $H(x,t)$ is not the conservative variable, $P(x,t)$ at next time step can be easily obtained using Eq. (82), that is, $\Delta\rho_i$ in Eq. (38) is

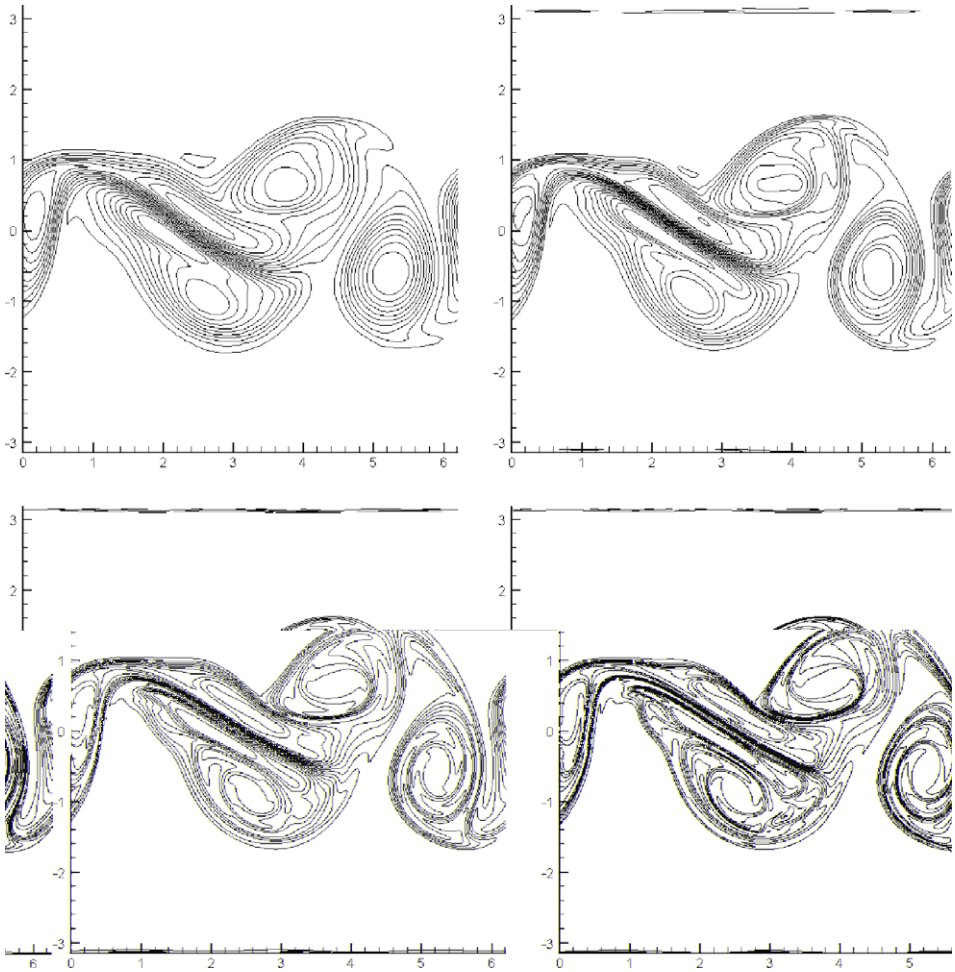

Fig. 32. Potential vorticity contour at $t = 2\pi$ with various gird numbers. (upper left) 100×100 grid, (upper right) 200×200 grid, (lower left) 400×400 grid and (lower right) 800×800 grid.

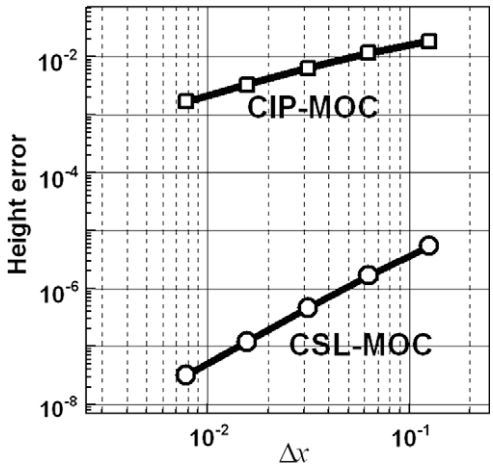

Fig. 33. Height error against grid resolution.

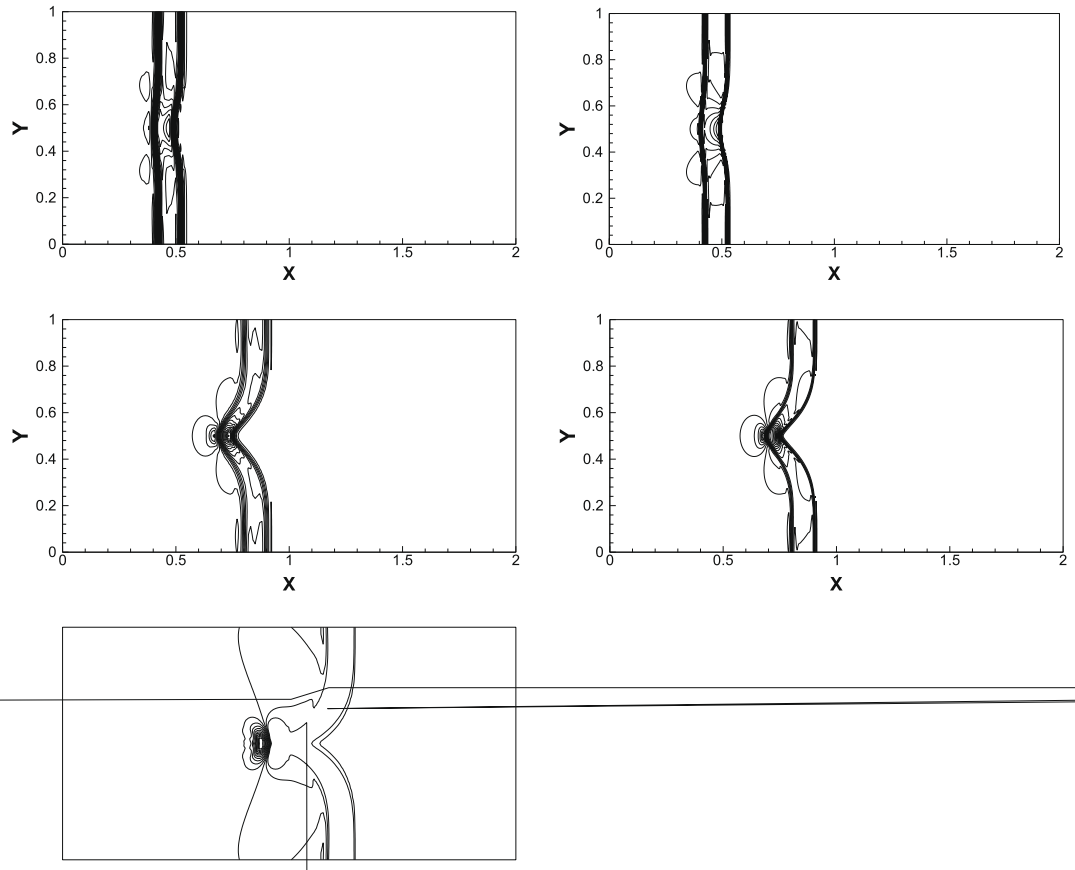

where ΔH is the initial perturbation and $H_c = 1.0$ is chosen. The gravitational acceleration is set to $g(= 1/Fr^2) = 9.81$. The number of mesh is 200 in $x \in [0, 2]$, then the grid size is $\Delta x = 0.01$. The CFL number is 0.32.

The first example is the equilibrium state ($\Delta H = 0$).

Fig. 34 shows the water level H and momentum hu at $t = 0.2$. It is seen that the equilibrium state is maintained within the computational round-off error without any numerical instabilities (this state is kept after $t = 0.2$ as well).

The second example is the small perturbation ($\Delta H = 0.001$). Some similar problems [33,34] have already been examined using the other schemes such as a fifth-order WENO scheme [13].

Fig. 35 shows the water level H and the momentum hu at $t = 0.2$. It can be seen that the numerical solution is accurate and almost in good agreement with other literatures. Unphysical waves and oscillations could occur around the hump after reflection if schemes would not preserve the discrete hydrostatic balance [35]. However, the CSL–MOC scheme makes shapes of rectangular waves traveling to the right and reflected to the left by the hump remained sharply, and no oscillation appears around the hump.

It is proved that the one-dimensional CSL–MOC scheme can preserve the discrete hydrostatic balance and the complete mass conservation with very small phase error and damping rate. Next, the two-dimensional version is also discussed.

We can rewrite the system equation (69) using the water level and velocities ($H(= h + z), u, v$) in two dimensions:

$$\frac{\partial H}{\partial t} + \frac{\partial (uH)}{\partial x} + \frac{\partial (vH)}{\partial y} = \frac{\partial (uz)}{\partial x} + \frac{\partial (vz)}{\partial y}, \tag{87}$$

$$\frac{\partial u}{\partial t} + u\frac{\partial u}{\partial x} + v\frac{\partial u}{\partial y} + g\frac{\partial H}{\partial x} = 0, \tag{88}$$

$$\frac{\partial v}{\partial t} + u\frac{\partial v}{\partial x} + v\frac{\partial v}{\partial y} + g\frac{\partial H}{\partial y} = 0. \tag{89}$$

We define line densities in both x- and y-directions (P_x, P_y) between grid points and the cell volume (P) in the middle of four grid points of the water level H as (see Fig. 16)

$$P_{xi,j} = \int_{x_i}^{x_{i+1}} H_{i,j}(x,y)dx = \sigma_{xi,j} + \frac{\Delta x}{2}(z_{i,j} + z_{i+1,j}), \tag{90}$$

$$P_{yi,j} = \int_{y_j}^{y_{j+1}} H_{i,j}(x,y)dy = \sigma_{yi,j} + \frac{\Delta y}{2}(z_{i,j} + z_{i,j+1}), \tag{91}$$

$$P_{i,j} = \int_{x_i}^{x_{i+1}} \int_{y_j}^{y_{j+1}} H_{i,j}(x,y)dx\,dy = \rho_{i,j} + \frac{\Delta x \Delta y}{4}(z_{i,j} + z_{i+1,j} + z_{i,j+1} + z_{i+1,j+1}), \tag{92}$$

and (P_x, P_y, P) are used in the two-dimensional CSL4 interpolation instead of (σ_x, σ_y, ρ).

The same directional splitting technique as Section 4 can be employed for time evolutions of all variables. In the x-directional operation, for example, (H, u) and averages ($\bar{H}(= P_y/\Delta y)$, see Eqs. (59)–(61), $\bar{u}$) can be updated by Eqs. (79) and (80), ($v, \bar{v}$) by Eq. (58) with $f = 0$, and (P_x, P) by Eqs. (18) and (83), respectively. The same procedure can be used in the y-direction, and time evolution in one time step is completed.

In order to verify the validity of the two-dimensional CSL–MOC scheme, a small perturbation of a two-dimensional steady-state lake problem given by LeVeque [33] is solved. The example has been used well to verify validities of numerical schemes [13,14,36].

The bottom topography is given by

$$z(x,y) = 0.8\exp(-5.0(x-0.9)^2 - 50.0(y-0.5)^2). \tag{93}$$

The initial conditions of the water level and the momentum in the x- and y-directions (H, hu, hv) are

$$H(x,y,t=0) = \begin{cases} H_c + \Delta H & \text{if } 0.05 < x < 0.15, \\ H_c & \text{otherwise}, \end{cases} \tag{94}$$

$$hu(x,y,t=0) = hv(x,y,t=0) = 0.0, \tag{95}$$

where $\Delta H = 0.01$ is the initial perturbation and $H_c = 1.0$ is chosen. The computational domain is $[0,2] \times [0,1]$, and two different uniform meshes with 200×100 and 600×300 are used. The gravitational acceleration is set to $g(= 1/Fr^2) = 9.81$. The CFL number is 0.32.

Shown in Fig. 36 are 30 uniformly spaced contour lines of the water level H at times $t = 0.12$, 0.24, 0.36, 0.48 and 0.60 with 200×100 meshes on the left side and 600×300 meshes on the right side.

As the initial perturbation propagates right and past the hump, the symmetric distortion by reflections and interactions on the surface wave appears due to the slow wave speed above the hump. It is observed that the CSL–MOC scheme is able to exactly simulate and reproduce complicated and symmetric structures as the other literatures.

References

[1] A. Arakawa, V.R. Lamb, A potential enstrophy and energy conserving scheme for the shallow water equations, Mon. Weather Rev. 109 (1981) 18–36.
[2] P.H. Lauritzen, E. Kaas, B. Machenhauer, A mass-conservative semi-implicit semi-Lagrangian limited-area shallow-water model on the sphere, Mon. Weather Rev. 134 (2006) 1205–1221.
[3] A. Staniforth, J. Côté, Semi-Lagrangian integration schemes for atmospheric models – a review, Mon. Weather Rev. 119 (1991) 2206–2223.

[4] G. Erbes, A semi-Lagrangian method of characteristics for the shallow-water equations, Mon. Weather Rev. 121 (1993) 3443–3452.
[5] T. Yabe, T. Aoki, A universal solver for hyperbolic equations by cubic-polynomial interpolation. I. One-dimensional solver, Comput. Phys. Commun. 66 (1991) 219–232.
[6] T. Yabe, T. Ishikawa, P.Y. Wang, A universal solver for hyperbolic equations by cubic-polynomial interpolation. II. Two- and three-dimensional solver, Comput. Phys. Commun. 66 (1991) 233–242.
[7] Y. Ogata, T. Yabe, Multi-dimensional semi-Lagarangian characteristic approach to the shallow water equations by the CIP method, Int. J. Comput. Eng. Sci. 5 (3) (2004) 699–730.
[8] B.P. Leonard, A.P. Lock, M.K. Macvean, Conservative explicit unstricted-time-step multidimensional constancy-preserving advection schemes, Mon. Weather Rev. 124 (1996) 2588–2606.
[9] M. Zerroukat, N. Wood, A. Staniforth, SLICE: a semi-Lagrangian inherently conserving and efficient scheme for transport problems, Quart. J. R. Meteorol. Soc. 128 (2002) 2801–2820.
[10] J. Thuburn, A fully implicit, mass-conserving, semi-Lagrangian scheme for the *f*-plane shallow-water equations, Int. J. Numer. Method Fluid 56 (2008) 1047–1059.
[11] R.D. Nair, B. Machenhauer, The mass-conservative cell-integrated semi-Lagrangian advection scheme on the sphere, Mon. Weather Rev. 130 (2002) 649–667.
[12] E. Kaas, A simple and efficient locally mass conserving semi-Lagrangian transport scheme, Tellus 60A (2008) 305–320.
[13] S. Noelle, N. Pankratz, G. Puppo, J.R. Natvig, Well-balanced finite volume schemes of arbitrary order of accuracy for shallow water flows, J. Comput. Phys. 213 (2006) 474–499.
[14] M. Lukáčová-Medvid'ová, S. Noelle, M. Kraft, Well-balanced finite volume evolution Galerkin methods for the shallow water equations, J. Comput. Phys. 221 (2007) 122–147.
[15] R. Akoh, S. Ii, F. Xiao, A CIP/multi-moment finite volume method for shallow water equations with source terms, Int. J. Numer. Method Fluid 56 (2007) 2245–2270.
[16] T. Yabe, F. Xiao, T. Utsumi, Constrained interpolation profile method for multiphase analysis, J. Comput. Phys. 169 (2001) 556–593.
[17] T. Yabe, R. Tanaka, T. Nakamura, F. Xiao, An exactly conservative semi-Lagrangian scheme (CIP–CSL) in one dimension, Mon. Weather Rev. 129 (2001) 332–344.
[18] R. Tanaka, T. Nakamura, T. Yabe, Constructing exactly conservative scheme in non-conservative form, Comput. Phys. Commun. 126 (2000) 232–243.
[19] T. Nakamura, R. Tanaka, T. Yabe, Multi-dimensional conservative scheme in non-conservative form, CFD J. 9 (2001) 437–453.
[20] T. Nakamura, R. Tanaka, T. Yabe, K. Takizawa, Exactly conservative semi-Lagrangian scheme for multi-dimensional hyperbolic equations with directional splitting technique, J. Comput. Phys. 174 (2001) 171–207.
[21] J. Stoker, Water Waves: The Mathematical Theory with Applications, Interscience, 1957.
[22] T. Utsumi, T. Kunugi, T. Aoki, Stability and accuracy of the cubic interpolated propagation scheme, Comput. Phys. Commun. 101 (1997) 9–20.
[23] S-J. Lin, R.B. Rood, Multidimensional flux-form semi-Lagrangian transport schemes, Mon. Weather Rev. 124 (1996) 2046–2070.
[24] Magdi M. Shoucri, Note: numerical solution of the shallow water equations, J. Comput. Phys. 63 (1986) 240–245.
[25] Y. Ogata, T. Yabe, Shock capturing with improved numerical viscosity in primitive Euler representation, Comput. Phys. Commun. 119 (1999) 179–193.
[26] T. Yabe, H. Mizoe, K. Takizawa, H. Moriki, H-N. Im, Y. Ogata, Higher-order schemes with CIP method and adaptive Soroban grid towards mesh-free scheme, J. Comput. Phys. 194 (2004) 57–77.
[27] E.F. Toro, Riemann Solvers and Numerical Methods for Fluid Dynamics, Springer, 1997.
[28] R.F. Warming, R.M. Beam, Upwind second-order difference schemes and applications in aerodynamics flows, AIAA J. 14 (9) (1976) 1241–1249.
[29] H. Takewaki, T. Yabe, Cubic-interpolated pseudo particle (CIP) method: application to nonlinear or multi-dimensional problems, J. Comput. Phys. 70 (1987) 355–372.
[30] D.G. Dritschel, L.M. Polvani, A.R. Mohebalhojeh, The contour-advective semi-Lagrangian algorithm for the shallow water equations, Mon. Weather Rev. 127 (1999) 1551–1565.
[31] R. Sadourny, Conservative finite-difference approximations of the primitive equations on quasi-uniform spherical grids, Mon. Weather Rev. 100 (1972) 136–144.
[32] C. Chen, F. Xiao, Shallow water model on cubed-sphere by multi-moment finite volume method, J. Comput. Phys. 227 (2008) 5019–5044.
[33] R.J. LeVeque, Balancing source terms and flux gradients in high-resolution Godunov methods: the quasi-steady wave-propagation algorithm, J. Comput. Phys. 146 (1998) 346–365.
[34] J.G. Zhou, D.M. Causon, C.G. Mingham, D.M. Ingram, The surface gradient method for the treatment of source terms in the shallow-water equations, J. Comput. Phys. 168 (2001) 1–25.
[35] S. Vukovic, L. Sopta, ENO and WENO schemes with the exact conservation property for one-dimensional shallow water equations, J. Comput. Phys. 179 (2002) 593–621.
[36] Y. Xing, C.W. Shu, High order finite difference WENO schemes for a class of hyperbolic systems with source terms, J. Comput. Phys. 208 (2005) 206–227.